

AD A111126

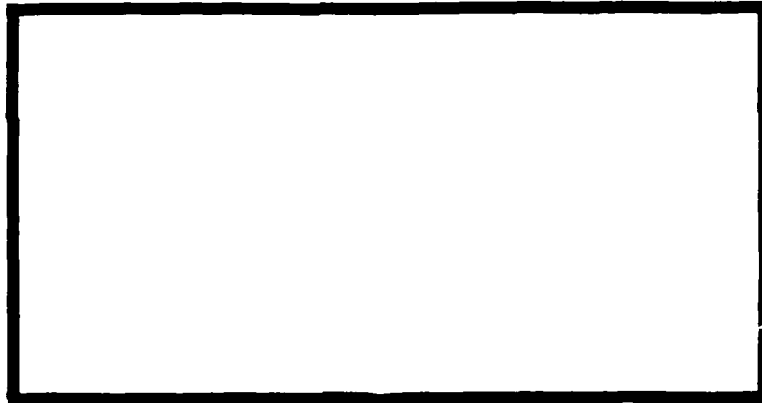
LEVEL II

1



DTIC
 ELECTE
 FEB 19 1982

E



DTIC FILE COPY

UNITED STATES AIR FORCE
 AIR UNIVERSITY
 AIR FORCE INSTITUTE OF TECHNOLOGY
 Wright-Patterson Air Force Base, Ohio

This document has been approved
 for public release and sale; its
 distribution is unlimited.

82 02 18 128

LEVEL II

①

THE VISCOPLASTIC CRACK GROWTH
BEHAVIOR OF A COMPACT TENSION
SPECIMEN USING THE BODNER-
PARTOM FLOW LAW

THESIS

AFIT/GAE/AA/81D-28 James W. Smail
Capt . USAF

Approved for public release; distribution unlimited.

Acknowledgments

I wish to express my gratitude to Dr. A.N. Palazotto for his guidance during the course of this study. Thanks also go to Dr. T. Nicholas of the Air Force Materials Laboratory, who provided many helpful suggestions and the computer resources needed to carry out my analysis.

Most of all, I wish to thank my wife, Diane, and daughter, Andrea, for their encouragement during the many long hours required to complete the research presented here. Without their support this project would have been impossible to complete.

James W. Smail

Contents

	<u>Page</u>
Acknowledgments	ii
List of Figures	v
List of Tables	viii
Abstract	ix
I. Introduction	1
Background	1
Approach	4
II. Theory	6
Plasticity	6
The Flow Curve	8
Bauschinger Effect	10
The von Mises Yield Criterion.	10
Prandtl-Reuss Equations.	12
Offset Plastic Strain.	14
Effects of Rate, Time, and Temperature	14
Creep.	15
Viscoplasticity.	18
Bodner's Viscoplastic Flow Law	19
III. The Computer Program	24
The Gauss-Seidel Iterative Solution Technique	24
Euler Extrapolation Scheme	29
Solution Procedure	30
Timestep Variation	33
The Yield Criterion.	34
IV. Experimental Procedure	35
Test Specimens	35
Apparatus and Instrumentation.	39
V. Finite Element Models.	41
Mesh Layout.	41

	<u>Page</u>
Comparison of Meshes	48
Effective Crack Lengths.	57
The Hybrid Experimental-Numerical Technique.	58
Crack Tip Node Release Method.	59
VI. Results and Discussion	65
Crack Growth Estimates	67
Crack Growth Criteria.	80
Critical Strain Criterion.	84
Critical Stress Criterion.	84
Accumulated Stress/Strain History.	89
VII. Summary and Conclusions.	93
Bibliography	96
Appendix: Finite Element Formulation.	99
Vita	103

List of Figures

<u>Figure</u>	<u>Page</u>
I-1 The Majority of Disks Have Useful Life After Retirement	3
II-1 Uniaxial Stress-Strain Curve.	9
II-2 Idealized Curve Showing the Three Stages of Creep.	16
II-3 Andrade's Analysis of the Competing Processes Which Determine the Creep Curve.	18
II-4 Uniaxial Viscoplastic Rheological Model	19
IV-1 Standard Compact Tension Specimen	36
IV-2 IN-100 Pancake Approximately 16 Inches in Diameter and 1.5 Inches Thick.	37
IV-3 ASTM 3-Point Averaging Method for Crack Lengths.	38
V-1 Finite Element, Constant Strain Model of the Compact Tension Specimen (Mesh 1).	42
V-2 Finite Element, Constant Strain Model of the Compact Tension Specimen (Mesh 2).	43
V-3 Finite Element, Constant Strain Model of the Compact Tension Specimen (Mesh 3).	44
V-4 Finite Element, Constant Strain Model of the Compact Tension Specimen (Mesh 4).	45
V-5 Uniform Mesh Ahead of Crack Tip	46
V-6 Definition of Terms for Use with Eqs. V1 and V-2.	49
V-7 Crack Mouth Opening Parameters for the Standard Compact Tension Specimen.	40
V-8 Finite Element Estimate of Stress Intensity Factor for Mesh 1 with an Applied Load of 2280 lbs	52

<u>Figure</u>	<u>Page</u>
V-9 Finite Element Estimate of Stress Intensity Factor for Mesh 2 with an Applied Load of 2280 lbs.	53
V-10 Finite Element Estimate of Stress Intensity Factor for Mesh 3 with an Applied Load of 2280 lbs.	54
V-11 Finite Element Estimate of Stress Intensity Factor for Mesh 4 with an Applied Load of 2280 lbs.	55
V-12 Load Line Displacement as a Function of Time for Specimen 7-1.	60
V-13 Load Line Displacement as a Function of Time for Specimen 7-2.	61
V-14 Load Line Displacement as a Function of Time for Specimen 7-3.	62
V-15 Load Line Displacement as a Function of Time for Specimen 7-4.	63
VI-1 Crack Growth as a Function of Time for Specimen 7-1.	69
VI-2 Crack Growth as a Function of Time for Specimen 7-2.	70
VI-3 Crack Growth as a Function of Time for Specimen 7-3.	71
VI-4 Crack Growth as a Function of Time for Specimen 7-4.	72
VI-5 Effective and HEN-VISCO Crack Lengths vs Time for Specimen 7-1	75
VI-6 HEN-VISCO Crack Length vs Time for Specimen 7-2	76
VI-7 Effective and HEN-VISCO Crack Lengths vs Time for Specimen 7-3	77
VI-8 Effective and HEN-VISCO Crack Lengths vs Time for Specimen 7-4	78
VI-9 Fracture Surface - Specimen 7-2.	81

<u>Figure</u>		<u>Page</u>
VI-10	Fracture Surface - Specimen 7-3.	82
VI-11	Fracture Surface - Specimen 7-4.	83

List of Tables

<u>Table</u>		<u>Page</u>
III-1	Effect of Overrelaxation Factor on Convergence	29
IV-1	Nominal Versus Actual K Values for Compact Tension Specimens	39
V-1	Comparison of Calculated and Finite Element Model Displacements	48
V-2	Comparison of Actual and Finite Element Mesh Stress Intensity Factors.	51
V-3	Estimated Crack Growth After 40 Minutes for Specimen 7-4.	56
VI-1	Crack Growth Estimates After 40 Minutes for Compact Tension Specimens	68
VI-2	Final Crack Lengths in Test Specimens.	79
VI-3	Average Plastic Strain at the Crack Tip as a Function of Crack Growth.	85
VI-4	Average Stress Perpendicular to the Crack Tip as a Function of Crack Growth	87
VI-5	Effective Stress as a Function of Crack Growth.	88
VI-6	Average Accumulated Stress History at Node Release for a Fixed Distance in Front of the Crack Tip	90
VI-7	Average Accumulated Stress History at Node Release for Plastic Zone in Each Specimen	91

Abstract

Creep crack growth in IN-100 was studied using a hybrid experimental-numerical procedure (HEN). This procedure couples displacement data generated during creep crack growth tests to a finite element model of the test specimen. A standard compact tension specimen geometry was used in all cases.

The computer program used herein is a two-dimensional plane stress/plane strain code that uses constant strain triangular elements and has the ability to release fixed nodes to simulate crack growth. This procedure is facilitated by using a Gauss-Seidel iterative solution technique that allows appropriate terms in the stiffness matrix to be changed between timesteps to accommodate changing boundary conditions due to crack growth. A variable timestep algorithm maximizes the timestep size during the analysis while maintaining good accuracy.

Constitutive equations proposed by Bodner and Partom were used to account for the nonlinear, viscoplastic material behavior exhibited by IN-100 at high temperatures. These equations were integrated through time by a linear Euler extrapolation technique.

Crack growth estimates generated with the HEN procedure were within 20 percent of the actual crack growth in

the test specimens after times ranging from 5-14 hours. Additionally, a critical stress and an accumulated stress history criterion for crack growth were both found to show promise. Both of these criteria merit further investigation.

THE VISCOPLASTIC CRACK GROWTH BEHAVIOR OF
A COMPACT TENSION SPECIMEN USING THE
BODNER-PARTOM FLOW LAW

I. Introduction

Background

With the introduction of the gas turbine engine, requirements developed for materials that could successfully operate in critically stressed parts such as turbine disks at a very high temperature. In this hostile environment, the phenomenon of creep (time dependent accumulation of plastic strain under constant stress) becomes important. Accumulation of creep strains can cause parts to deform beyond design limits. Also, undetected creep crack growth could result in rupture of a disk. To further complicate matters, changes in throttle settings during flight along with engine starts and shutdowns at the beginning and end of each mission induce cyclic stresses that bring the fatigue process into play. However, most mission profiles include long dwell times at constant engine speed, such as during high altitude cruise. During such periods the failure process is dominated by creep. Therefore, a separate investigation of creep crack growth is warranted and would contribute to a better understanding of the combined failure process.

Generally, creep deformation and rupture are initiated

at the grain boundaries and proceed by sliding and separation. Thus, creep rupture failures are intercrystalline in contrast, for example, to the transcrystalline failure surfaces exhibited by room temperature fatigue failures. Although creep is a plastic flow phenomenon, the intercrystalline failure path gives a rupture surface that has the appearance of brittle fracture. Creep rupture typically occurs without necking and without warning. Current state of the art knowledge does not permit a reliable prediction of creep rupture properties on a theoretical basis. Further, there seems to be little or no correlation between the creep properties of a metal and its room temperature mechanical properties (1).

Since failure of a turbine disk could result in the loss of a multi-million dollar aircraft and its crew, current Air Force policy is to remove all disks in a given population from service at the time where 1 in 1000 could be expected to have initiated a short (0.03 in) fatigue crack (2). From a safety standpoint, this policy works well. However, by definition 99.9 percent of the retired disks still have useful life remaining at the time they are removed from service. As shown in Fig. I-1, over 80 percent of the disks have at least ten lifetimes remaining and over 50 percent have at least 25 lifetimes remaining.

If we could accurately predict the remaining life of a turbine disk that contained a subcritical flaw, many parts that are currently retired could be kept in service. Parts

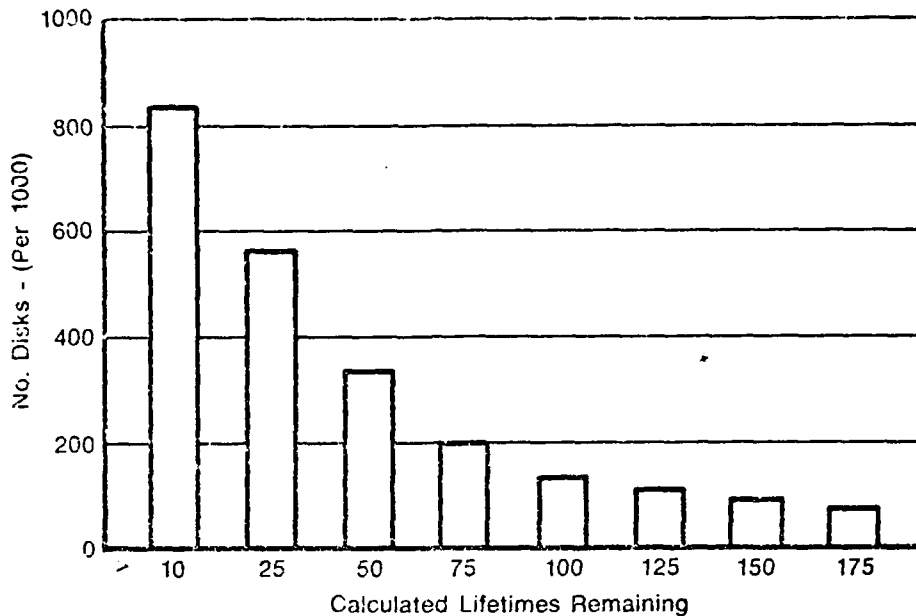


Fig. I-1. The Majority of Disks Have Useful Life After Retirement (2)

would be inspected at intervals determined by the ability to detect flaws of some given size and a fracture mechanics calculation of the remaining life with a crack just small enough to have been missed during inspection. This procedure would be repeated until the disk failed to meet the requirements for a return to service, at which time it would be retired. The Air Force calls such a program retirement for cause and is currently studying its feasibility for use in the F-100 engine program. If we assume a 15-year engine lifetime, a retirement for cause program could result in engine life cycle cost savings of about \$249 million (2).

Approach

This thesis concentrates on creep crack growth in IN-100, an advanced, nickel based superalloy that is used as a turbine disk material in the F-100 engine. Experimental creep crack tests were conducted at a fixed temperature of 1350 F (732 C). The tests were modeled using the finite element method and a sophisticated, nonlinear, time dependent set of constitutive equations called the Bodner-Partom viscoplastic flow law (3; 4; 5; 6). This flow law was integrated through time using a linear Euler extrapolation technique (7) and incorporated into the finite element model by the residual force method (8). The computer program used was an in-house code named VISCO that was developed by Hinnerichs (9). VISCO uses constant strain triangular elements and has the ability to release fixed nodes to simulate crack growth. This procedure is facilitated by using a Gauss-Seidel iterative solution technique (10; 11; 12) that avoids costly matrix factorization and allows appropriate terms in the stiffness matrix to be changed between timesteps to accommodate changing boundary conditions due to crack growth. Additionally, a variable timestep algorithm is used to allow the timestep to increase or decrease as a function of the rate of change in stress and strain. This allows us to model creep crack growth by providing the ability to transition from very small timesteps during load application or node releases to very large timesteps during pure creep.

The primary goal of this study was to determine if

experimentally measured, far field displacements could be used to predict creep crack growth in the test specimens. A secondary goal was to examine other parameters such as the stress, strain and stress intensity factor at the crack tip as criteria for crack growth. Hopefully, such analysis will contribute to the understanding of creep crack growth and help make a retirement for cause program for jet engine turbine disks possible.

II. Theory

This section contains a brief review of the theory of plasticity, definitions of important terms, and an introduction to the material model used in conducting this study.

Plasticity

Plasticity can be defined as permanent deformation of a material by the application of stresses which are greater than those necessary to cause yielding (13). If yielding has not occurred, we can use simple linear elastic constitutive equations such as Hooke's law to perform any required analysis. However, once yielding occurs, we must use a set of plastic constitutive equations. Generally, such equations are nonlinear and much more complicated than those used in elasticity.

Given the above definition of plasticity, a logical question to ask would be--How do we determine when yielding occurs? If we are interested in a case of simple tension, the yield stress is easily determined from a uniaxial tension test where we measure a specimen's elongation under a constantly increasing load. The ratio of the load on the specimen to the original cross sectional area is defined as the nominal stress and the ratio of the change in length to the original length is defined as the conventional or engineering strain. These quantities are expressed in

equation form as follows:

$$\text{stress: } \sigma = P/A_0 \quad (\text{II-1})$$

$$\text{strain: } \epsilon = \frac{l-l_0}{l_0} \quad (\text{II-2})$$

where P is the applied load, A_0 is the original area, l is the current length, and l_0 is the original length.

Alternatively, stress may be defined as the ratio of load to the instantaneous cross sectional area, and strain may be defined as the ratio of the change in length to the instantaneous length. Since the length of the specimen is constantly changing, it is necessary to express this type of strain by considering only an infinitesimal amount of deformation where we can consider the length to be constant (14). Thus, the infinitesimal strain is expressed as

$$d\epsilon_T = \frac{dl}{l} \quad (\text{II-3})$$

and our stress is expressed as

$$\sigma = P/A \quad (\text{II-4})$$

These are called the true stress and time strain. To find the expression for a finite amount of true strain, we simply integrate between the original length and the current length such that :

$$\epsilon_T = \int_{l_0}^l \frac{dl}{l} = \ln \frac{l}{l_0} \quad (\text{II-5})$$

Due to the nature of this expression, true strain is often

called logarithmic strain.

The relationship between true strain and conventional strain is

$$\epsilon_T = \ln(1 + \epsilon) \quad (\text{II-6})$$

True strain and conventional strain are essentially equal when the strains are small, but they diverge as the strains increase.

Henceforth, the terms stress and strain will be understood to mean nominal stress and conventional strain. True stress and true strain will be labeled as such.

The Flow Curve. If we make a plot of stress versus strain for a uniaxial tension test, a curve similar to that shown in Fig. II-1 will result for most, but not all materials. The slope of the linear portion of this curve is called the modulus of elasticity, E . In this region, stresses and strains are related by Hooke's law:

$$\epsilon = \sigma/E \quad (\text{II-7})$$

The theory of plasticity deals with the behavior of materials in the region beyond which Hooke's law is no longer valid (15).

Point A, where the curve deviates from linearity is called the proportional limit, while the maximum stress that the material can withstand without experiencing any plastic deformation is called the elastic limit. The elastic limit is not easy to determine, so we usually specify the limit of elastic behavior as some small amount of permanent deformation,

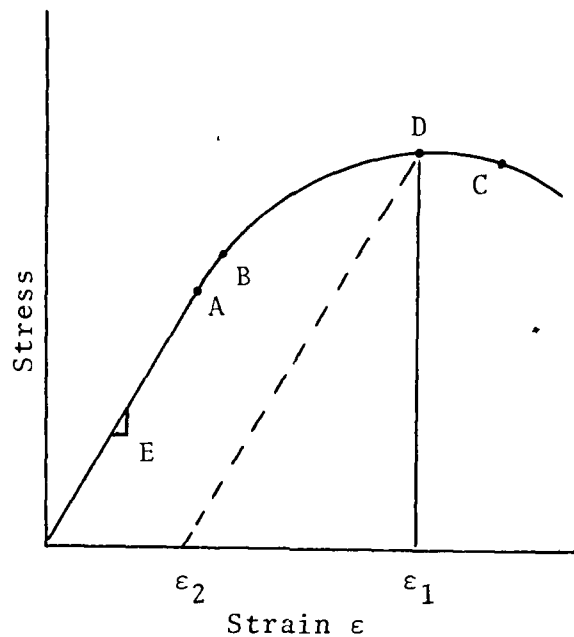


Fig. II-1. Uniaxial Stress-Strain Curve

generally a strain of 0.2 percent (15). The stress that will produce this amount of permanent deformation is called the yield stress and is labeled B in Fig. II-1.

Whenever the elastic limit is exceeded, plastic deformation takes place and the strain begins to increase at a greater rate. However, increased deformation must be accompanied by an increase in load because plastic flow increases the yield stress of most metals. This effect is called strain hardening, and continues until reaching point C. The stress at this point is called the ultimate tensile strength. Beyond this the area of a ductile specimen decreases rapidly until fracture occurs.

If we stress the metal to some point D and then unload

it, the strain will decrease from ϵ_1 to ϵ_2 . The difference $\epsilon_1 - \epsilon_2$ is called the elastic strain. However, ϵ_2 is not all permanent plastic strain. Depending on the material and the temperature, a small additional amount of strain may disappear with time. This is called anelastic behavior. In most cases, the effects of anelastic behavior are small and it is usually ignored in mathematical theories of plasticity (15).

Bauschinger Effect. If, instead of conducting a tensile test, we run a compression test and then plot a curve of stress versus strain, the result may be quite different from that shown in Fig. II-1. However, if we plot true stress versus true strain for both tests, the two curves will be nearly identical (16). For one thing, the yield stress in tension and compression will be about the same. Note that this similarity only holds for specimens that have not been previously deformed. For example, if we first deform a specimen in tension and then run a compression test on the same specimen, the yield point in compression will be considerably less than that in the tensile test. This phenomenon is called the Bauschinger effect and is present whenever there is a reversal of a stress field. This effect can become very important in cyclic loading problems. Unfortunately, it is usually ignored because it complicates the problem (16).

The von Mises Yield Criterion. For multiaxial stress states the onset of plasticity is not as easily defined as

in the uniaxial case. There may be many combinations of stresses that result in plastic deformation. Therefore, we must develop some other yield criterion to replace the uniaxial yield stress in this case.

Many criteria have been proposed, but we will focus on the one proposed by von Mises. The reader interested in a more thorough discussion can find information in Mendelson's text (16) or in numerous other books on plasticity.

The von Mises yield criterion is also called the distortion energy theory. This theory states that yielding begins when the distortion energy equals the distortion energy that exists when yielding occurs in uniaxial tension.

If we let J_2 be the second invariant of the deviatoric stress tensor, and G be the shear modulus, the distortion energy, U_d , is defined as

$$U_d = \frac{1}{2G}J_2 \quad (\text{II-8})$$

In terms of the principal stresses,

$$J_2 = \frac{1}{6} [(\sigma_1 - \sigma_2)^2 + (\sigma_2 - \sigma_3)^2 + (\sigma_3 - \sigma_1)^2] \quad (\text{II-9})$$

At the yield point in uniaxial tension Eq (II-9) reduces to

$$J_2 = \frac{1}{3}\sigma_0^2 \quad (\text{II-10})$$

where σ_0 is the uniaxial yield stress. Thus, yielding occurs when

$$\frac{1}{2} [(\sigma_1 - \sigma_2)^2 + (\sigma_2 - \sigma_3)^2 + (\sigma_3 - \sigma_1)^2] = \sigma_0^2 \quad (\text{II-11})$$

In other words, the von Mises criterion will predict yielding when J_2 reaches the value of J_2 at yield in a uniaxial tension test.

An important point to remember here is that the deviatoric stress tensor does not contain hydrostatic stresses. Therefore, the von Mises yield criterion does not predict yielding for states of pure hydrostatic stress, no matter how large the stresses may be. This is in agreement with experimental results obtained by Bridgman (17; 18), who showed that hydrostatic pressure has negligible effect on yield stress until extremely high pressures are reached. This fact allows us to consider only the deviatoric components of the stress tensor during plastic flow. An effect related to this is that plastic deformation does not appreciably change either volume or density in metals, so most metals can be considered incompressible in the plastic range (16).

Prandtl-Reuss Equations. Now that we have a criterion that tells us when plastic flow begins, we need a set of equations to express the relationship between stress and strain in the plastic region. In classical plasticity, this requirement is satisfied by the Prandtl-Reuss equations which, in incremental form, are:

$$d\epsilon_{ij}^P = d\lambda S_{ij} \quad (II-12)$$

where ϵ_{ij}^p are the components of the plastic strain tensor, S_{ij} are the components of the deviatoric stress tensor, and λ is a positive scalar. The instantaneous value of λ is left to the inventiveness of the user of these equations (8).

Given an expression for $d\lambda$, we can find the plastic strain corresponding to the stress state at any particular instant. One way to express it is (16):

$$d\lambda = \frac{3}{2} \frac{d\epsilon_p}{\sigma_e} \quad (\text{II-13})$$

where

$$\sigma_e \equiv \sqrt{3J_2} \quad (\text{II-14})$$

$$d\epsilon_p = \sqrt{2} d\gamma_0^p \quad (\text{II-15})$$

and γ_0^p is the octahedral shear strain. We call σ_e the effective stress and ϵ_p the effective plastic strain.

Using this form for $d\lambda$, the Prandtl-Reuss equations are

$$d\epsilon_{ij}^p = \frac{3}{2} \frac{d\epsilon_p}{\sigma_e} S_{ij} \quad (\text{II-16})$$

A comparison of the effective stress, Eq. (II-14), with the von Mises yield criterion, Eq. (II-10), shows that when yielding begins $\sigma_e = \sigma_0$. In other words, the effective stress takes on the same form as the von Mises yield criterion. Since Eq. (II-16) makes use of the effective stress, this form of the Prandtl-Reuss equations implies the von Mises yield criterion (16). However, the form of $d\lambda$ depends on the plastic flow law that is chosen by the user, so there

may be occasions when something other than the von Mises yield criterion is used. We will look at another way to express $d\lambda$ later.

Offset Plastic Strain. As previously mentioned, it is customary to define plastic strain as the permanent strain left in a specimen after the load is removed. However, this definition is cumbersome for experimental work where the specimen cannot be unloaded every time we want to know what the plastic strain is. Therefore, in all of the results presented in this thesis, the plastic strain will be defined as the difference between the total strain and the elastic strain:

$$\epsilon^P = \epsilon - \sigma/E \quad (II-17)$$

Plastic strain defined in this way is called offset plastic strain (14) since it is the offset distance from the linear elastic line.

Effects of Rate, Time, and Temperature. The discussion of plastic behavior presented so far has been quite idealized. Actually, there are certain deviations from this behavior due to the effects of such things as rate of load application, temperature, and time.

In most metals, high rates of load application result in less plastic flow than low load rates. This is called rate sensitivity. The magnitude of this effect is relatively minor at room temperature, but it increases rapidly as temperature increases (19).

Besides influencing rate sensitivity, temperature affects many other properties of a given material. Usually, the ultimate tensile strength, proportional limit, and modulus of elasticity decrease as temperature increases. Time rates of change of deformation and stress also become more important at higher temperatures. This suggests the idea of plasticity as a matter of viscous flow in a fluid (20; 21), which is the viewpoint adopted in this thesis.

Three important, time dependent processes are recovery, relaxation, and creep. Recovery is defined as the restoration of the physical properties of a cold worked metal without any observable change in the microstructure (15). This effect results in a reduction in strain hardening over time in materials that have been plastically deformed at high temperatures.

If a specimen is deformed and then held in a fixed position, the stresses within the specimen will gradually diminish (19). This is called relaxation. On the other hand, if we apply a constant load to a specimen, deformation continues to increase with time. This increase in strain in the course of time under constant stress is called creep. Creep and recovery are complementary processes and are most pronounced at high temperatures. However, their effects never completely disappear, even at very low temperatures (14).

Creep. Since a creeping metal is the focus of this thesis, the phenomena merits a closer look.

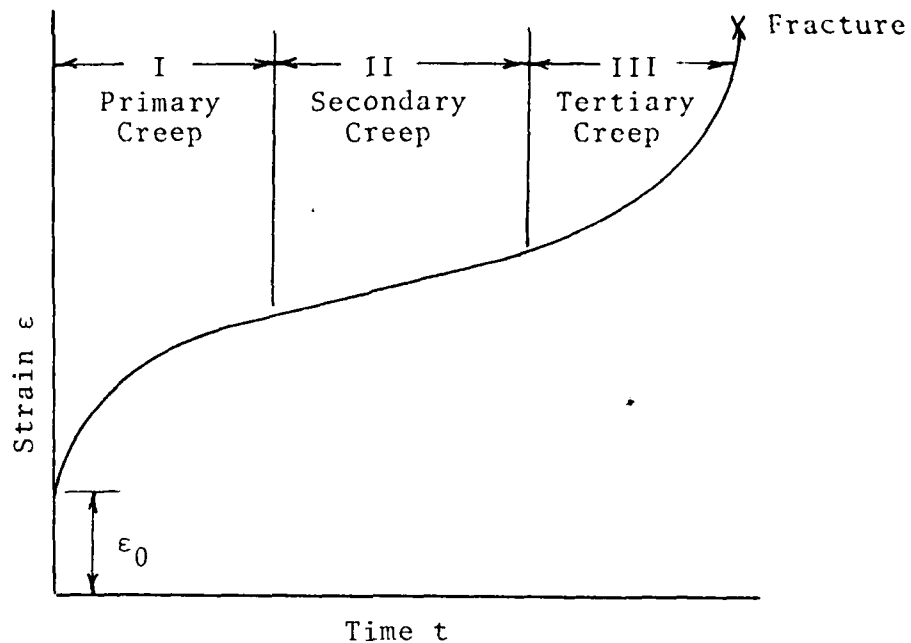


Fig. II-2. Idealized Curve Showing the Three Stages of Creep

A creep test may be conducted by applying a constant load to a specimen held at a constant temperature and then measuring the strain as a function of time. The elapsed time of such tests may exceed several months, while some tests have been run for more than ten years (15).

An idealized creep curve generally looks like the one shown in Fig. II-2. As shown, these curves are commonly divided into three regions called primary, secondary and tertiary creep, or stage I, stage II and stage III creep. The slope of the curve is referred to as the creep rate. After an initial rapid elongation, ϵ_0 , we begin the primary stage of creep. During primary creep, the creep rate decreases until it reaches a minimum rate that is maintained

for the duration of secondary creep. Finally, in the tertiary stage, the creep rate begins to increase rapidly and, eventually, failure occurs.

Research in the phenomenon of creep was pioneered by Andrade (21; 22). He considered the first two stages of the constant stress creep curve to be a superposition of the three phenomena illustrated in Fig. II-3. After a sudden strain due to load application, a transient component that decreases with time is combined with a viscous component that progresses at a constant rate. Since the primary stage of creep represents a region of decreasing creep rate, it is dominated by transient creep. During this stage, the creep resistance of the material increases by virtue of its own strain hardening (15).

Secondary creep represents a balance between strain hardening and recovery (19), such that the creep rate is essentially constant.

The reasons for the rapid acceleration of the creep rate during tertiary creep are not well understood. It is unlikely that tertiary creep is due solely to necking of the specimen, since many materials fail in creep of strains which are too small to produce necking. Tertiary creep is more probably the result of structural changes occurring in the metal. Evidence has been found for void formation and extensive crack formation during this stage (15). Due to the complexity of tertiary creep and the fact that primary and secondary creep often cover most of a specimen's useful

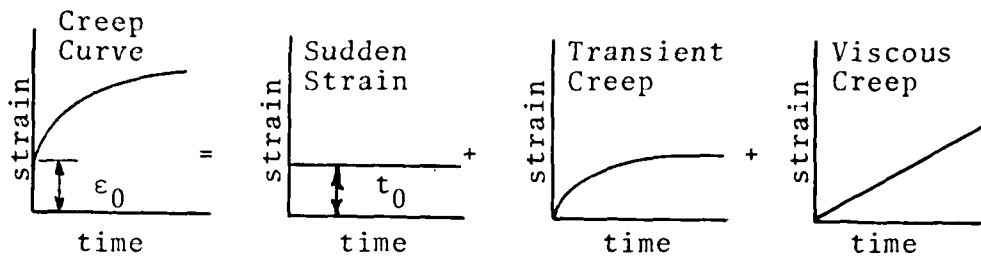


Fig. II-3. Andrade's Analysis of the Competing Processes Which Determine the Creep Curve (15)

life, most analytical models do not include tertiary creep.

Viscoplasticity. It is common practice to separate creep and plasticity into separate categories. Creep includes all time effects and results in strains being developed at a finite rate. Plasticity develops plastic strains instantaneously, and time does not enter directly into consideration. Physically, creep and plasticity cannot be treated separately since only the combined effect is measurable. Also, the concept of instantaneous development of permanent strain is at variance with experiment and plasticity is, at best, only a convenient mathematical fiction (7). The combination of these two phenomena into a unified model is called viscoplasticity (7; 23).

A model that includes purely elastic as well as viscoplastic behavior is called elasto-viscoplastic. In such a model, only the elastic strains are allowed to accumulate instantaneously. The rate of the time dependent strains depends on how much the applied stress exceeds the yield stress. Three uniaxial viscoplastic rheological

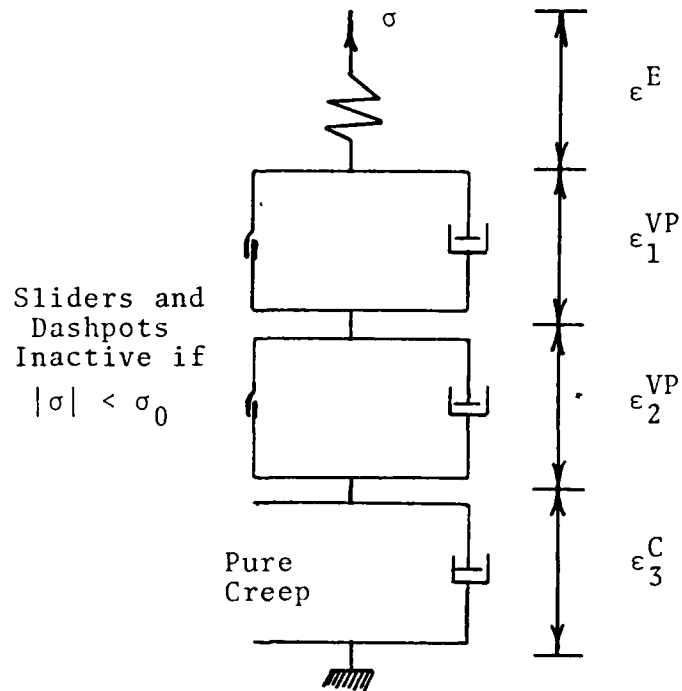


Fig. II-4. Uniaxial Viscoplastic Rheological Model (7)

models in series are shown in Fig. II-4. In instantaneous load application, only elastic straining of the spring takes place. The excess $\sigma - \sigma_0$ is taken by the dashpots, which results in a time variable strain. By placing more than one viscoplastic model in series, as is shown in Fig. II-4, a very general uniaxial behavior can be introduced (7).

Bodner's Viscoplastic Flow Law

A theory that accounts for viscoplastic behavior as well as rate sensitivity and strain hardening effects is the Bodner-Partom viscoplastic flow law (3; 4; 5; 6). An

essential feature of this formulation (henceforth referred to as the Bodner model) is that the total deformation rate is assumed to be separable into elastic and inelastic components:

$$\dot{\epsilon}_{ij} = \dot{\epsilon}_{ij}^E + \dot{\epsilon}_{ij}^P \quad (\text{II-18})$$

where the elastic strain rate, $\dot{\epsilon}_{ij}^E$, is related to the stress rate through the time derivative of Hooke's law. A yield criterion is not required since both strain rate components are considered non-zero for all non-zero stresses.

By assuming incompressibility and isotropy, the plastic strain rate can be expressed in the form of the Prandtl-Reuss equations of classical plasticity. Written in terms of the strain rate, these become:

$$\dot{\epsilon}_{ij}^P = \dot{e}_{ij}^P = \lambda S_{ij} \quad (\text{II-19})$$

where \dot{e}_{ij}^P is the deviatoric plastic strain rate tensor and the other quantities remain as previously defined. As noted earlier, the form of λ depends on the flow law selected. Bodner expressed λ as a function of J_2 by squaring Eq (II-19) to get

$$\lambda^2 = D_2^P / J_2 \quad (\text{II-20})$$

where $D_2^P = \frac{1}{2} \dot{\epsilon}_{ij}^P \dot{\epsilon}_{ij}^P$ is the second invariant of the plastic strain rate tensor and $J_2 = \frac{1}{2} S_{ij} S_{ij}$ is the second invariant of the deviatoric stress tensor.

A principle feature of Bodner's theory is the

consideration that D_2^P is a function of J_2 . This hypothesis is partially motivated by the extensive work in the field of dislocation dynamics, which has shown that the dislocation velocity and, therefore, the uniaxial plastic strain rate is a function of the stress (3). The exact form of this relationship is expressed as

$$D_2^P = D_0^2 \exp \left[- \left(\frac{Z^2}{3J_2} \right)^n \frac{n+1}{n} \right] \quad (\text{II-21})$$

The constant D_0 is the limiting value of the plastic strain rate in shear. This value can be arbitrarily chosen and is usually taken to be the same large number for all materials. Except for very high rates of straining, a value of $D_0 = 10^4 \text{sec}^{-1}$ is generally adequate.

The exponent n is a rate sensitivity parameter and influences the overall level of the stress-strain curves. Decreasing n results in increased rate sensitivity and a lowering of the stress-strain curves. It is a fundamental material constant and is not dependent on the loading history. Bodner introduced the factor $(n+1)/n$ at an early stage in the development of his equations for numerical purposes (4). It is not basically necessary, and dropping it would only result in a change in some of the material constants, not a change in the model's behavior.

Physically, Z can be interpreted as a macroscopic hardening parameter that controls the resistance to inelastic flow. In order to model strain hardening, Z must be made

dependent on the deformation history of the material. Thus, it is assumed to be a function of the plastic work, W_p , such that

$$Z = Z(W_p) = Z_1 + (Z_0 - Z_1) \exp(-mW_p/Z_0) \quad (\text{II-22})$$

The function $Z = Z(W_p)$ is a basic material property which directly influences the plastic stress-strain relations.

In Eq (II-22), Z_1 is the maximum expected value of Z , Z_0 is the initial value of Z corresponding to the reference point from which we measure plastic work, and m is a material constant that controls the rate of work hardening. The parameter Z_1 is necessary to set an upper bound on Z , because without it D_2^P would approach zero for large values of plastic work. This would correspond to a reversion to completely elastic behavior and an unrealistic upward turn in the stress-strain curve (3). Although Z_1 is taken to be a constant in this exercise, cyclic loading cases can be handled by making Z_1 dependent on loading history (14).

Generally, the plastic work is defined as

$$W_p = \int S_{ij} \dot{\epsilon}_{ij}^P dt \quad (\text{II-23})$$

However, at high temperatures it is generally necessary to consider the thermal recovery of hardening generated by plastic deformation. This is done by redefining the plastic work as follows (9).

$$W_p = \int S_{ij} \dot{\epsilon}_{ij}^P dt + \int \frac{\dot{z}_{rec}}{m(Z_1 - Z)} dt \quad (\text{II-24})$$

where

$$\dot{z}_{\text{rec}} = -A\left(\frac{Z-Z_2}{Z_1}\right)^r Z_1 \quad (\text{II-25})$$

Z_2 is the value of Z for the completely non-work hardened state and, therefore, represents the minimum hardness we would expect to see in a particular material at a given temperature. A and r are material constants chosen to make the model's behavior match creep test data. It should be noted that the inclusion of this recovery term is necessary if we wish the model to represent secondary creep.

The constants in the Bodner model are temperature dependent, but this can be effectively suppressed by evaluating the constants at the specific temperature of interest. In this case, Stouffer (6) determined that the following values of the constants best fit the behavior of IN-100 at 1350 F.

$$D_0 = 10^4 \text{ sec}^{-1} \text{ (assumed)}$$

$$n = 0.7$$

$$Z_0 = 915.0 \text{ KSI (6304 MPa)}$$

$$Z_1 = 1015.0 \text{ KSI (6993 MPa)}$$

$$Z_2 = 600 \text{ KSI (4134 MPa)}$$

$$m = 2.57 \text{ KSI}^{-1} \text{ (.37273 MPa}^{-1}\text{)}$$

$$A = 1.9 \times 10^{-3} \text{ sec}^{-1}$$

$$r = 2.66$$

$$(1 \text{ Kbar} = 100 \text{ MPa} = 14.504 \text{ KSI})$$

III. The Computer Program

The computer program used in this exercise was an in-house code named VISCO (9). It is a two-dimensional, plane stress/plane strain finite element program that uses constant strain triangular elements. In addition to the Bodner-Partom viscoplastic flow law, VISCO incorporates the Malvern (overstress) flow law and Norton's law for secondary creep. The user has the option of selecting any of these three models individually or using a combination of the Malvern and Norton models. We will be concerned only with the Bodner model. The user interested in a discussion of the other models should consult reference 9.

The Gauss-Seidel Iterative Solution Technique

In finite element analysis, the equilibrium equations are expressed in matrix form as

$$[K]\{U\} = \{P\} \quad (III-1)$$

where $[K]$ is a symmetric, positive definite, $n \times n$ stiffness matrix, $\{U\}$ are the nodal displacements, and $\{P\}$ the applied loads. Most large-scale computer programs use some form of Gaussian elimination to solve Eq (III-1) (10). Such methods are called direct techniques, whereas iterative processes are called indirect techniques. Direct solutions usually involve costly matrix factorizations. However, once the

factorization is complete, solution of the equations is relatively cheap. Also, the factorization does not have to be repeated if we wish to change the right-hand side of Eq (III-1). Thus, several different load cases can be handled quickly and efficiently. For this reason, direct techniques are currently favored over indirect techniques.

Iteration does have some advantages however. In general, an iterative solution technique requires less central memory storage and eliminates matrix factorization, which is the most costly part of a direct solution. The disadvantages are: the lack of knowledge on how many iterations are required to achieve an acceptable solution (often hundreds or thousands of iterations are required); the method fails in indefinite or unsymmetric problems; if the right-hand side is changed, no advantage can be taken of a previous solution as the whole iteration process must be repeated. The disadvantages usually far outweigh the advantages of iterative techniques (11). However, in a program like VISCO where we want to simulate crack growth, the stiffness matrix must be changed every time a node is released. Use of a direct technique would require us to repeat costly matrix factorizations to accommodate the changing boundary conditions due to crack growth. With an iterative technique, applicable terms in the stiffness matrix are easily changed between timesteps and factorization is avoided. Therefore, VISCO uses the Gauss-Seidel iterative technique with over-relaxation.

This technique is implemented in the following manner (9). Consider Eq (III-1), rewritten as

$$[K]\{U\} = \begin{bmatrix} S_{XX} & S_{XY} \\ S_{YX} & S_{YY} \end{bmatrix} \begin{Bmatrix} U_x \\ U_y \end{Bmatrix} = \begin{Bmatrix} P_x \\ P_y \end{Bmatrix} \quad (\text{III-2})$$

where U_x and U_y are the displacements in the x and y directions, and P_x and P_y are the applied loads in the x and y directions. If the matrix $[K]$ has dimensions $n \times n$, the submatrices S_{XX} , S_{XY} , S_{YX} and S_{YY} will have dimensions $n/2 \times n/2$. However, by storing only the non-zero terms, we can considerably reduce storage requirements. In VISCO we assume that the displacements at any one node can be determined by considering only the nodes that are directly connected to it. Further, in the Gauss-Seidel technique, the displacement vector may be found by considering only one node at a time. If we specify that a maximum of eight nodes may be connected to any given node, we will never need to know more than nine terms at once. Thus, the four submatrices can be compacted to a matrix which is $n/2 \times 9$. Since triangular elements tend to develop undesirable aspect ratios if more than eight nodes are connected to any one node (9), our eight-node limit is not very restrictive.

In order to help retrieve the proper terms from the compacted submatrices, VISCO uses a matrix NP and a vector NAP . The dimension of NAP is $n/2$ and the dimensions of NP are $n/2 \times 9$. The number of nodes connected to node I is stored in $NAP(I)$ while $NP(I,J)$ stores the location in the

submatrices of the terms associated with the J^{th} node point connected to node I. Note that for node I, J may go from 1 to NAP(I).

Using the above notation, the equilibrium equations for the I^{th} node point are written as:

$$\begin{bmatrix} \text{SXX}(I,1) & \text{SXY}(I,1) \\ \text{SYX}(I,1) & \text{SYY}(I,1) \end{bmatrix} \begin{Bmatrix} U_x(I) \\ U_y(I) \end{Bmatrix} = \quad , \quad (\text{III-3})$$

$$\begin{Bmatrix} P_x(I) \\ P_y(I) \end{Bmatrix} - \sum_{J=2}^{\text{NAP}(I)} \begin{bmatrix} \text{SXX}(I,J) & \text{SXY}(I,J) \\ \text{SYX}(I,J) & \text{SYY}(I,J) \end{bmatrix} \begin{Bmatrix} U_x(J) \\ U_y(J) \end{Bmatrix}$$

For the sake of brevity, let the right-hand side of Eq (III-3) be defined as $\begin{Bmatrix} \text{FRX} \\ \text{FRY} \end{Bmatrix}$. Solving for the displacements at node I gives:

$$\begin{Bmatrix} U_x(I) \\ U_y(I) \end{Bmatrix} = \begin{bmatrix} \text{SXX}(I,1) & \text{SXY}(I,1) \\ \text{SYX}(I,1) & \text{SYY}(I,1) \end{bmatrix}^{-1} \begin{Bmatrix} \text{FRX} \\ \text{FRY} \end{Bmatrix} \quad (\text{III-4})$$

Note that solving Eq (III-3) only requires the inversion of a 2x2 matrix. Since these terms in the submatrices are not used for anything else, we can do all our inversions in advance and store the results in the original submatrix locations.

As a starting point in the iterations, we use an initial estimate for the displacements which, for lack of a better value, may be a null vector. After the displacements at a node are calculated from Eq (III-4), these values are substituted for the previous estimate and the displacements

of the next node are calculated. An iteration is complete when we have calculated the displacements of each node point. Next, we calculate the change in displacements from the previous iteration and use these to compute a tolerance limit that is, in turn, used to test for convergence. In VISCO the tolerance limit is called SUM and is defined as:

$$\text{SUM} = \sum_{I=1}^{n/2} [|\Delta U_x(I) * \text{SXX}(I,1)| + |\Delta U_y(I) * \text{SYY}(I,1)|] \quad (\text{III-5})$$

where ΔU_x and ΔU_y are the change in displacements between iterations m and $m+1$. If SUM becomes less than a specified value, θ , we assume we have converged to the correct solution and iterations are stopped. The value of θ must be determined by considering the desired accuracy and the number of iterations required for convergence. Smaller values of θ produce more accurate solutions, but require more computer time to solve for a given problem than larger values of θ .

An iterative solution for the displacements is obtained after each timestep, but convergence is usually much faster than for the first set of iterations because we can use the displacements from the previous timestep as our initial estimate. Often, the convergence process can be further speeded up by employing an overrelaxation factor. In this case, the new displacements for iteration m would be:

$$\begin{Bmatrix} U_x(I) \\ U_y(I) \end{Bmatrix}^m = \begin{Bmatrix} U_x(I) \\ U_y(I) \end{Bmatrix}^{m-1} + \text{XFAC} \begin{Bmatrix} \Delta U_x(I) \\ \Delta U_y(I) \end{Bmatrix}^m \quad (\text{III-6})$$

where the superscripts refer to the iteration number and XFAC is the overrelaxation factor. The optimum value of XFAC generally lies between 1.3 and 1.9 (10). Table III-1 illustrates the effect of the overrelaxation factor on convergence in solving for the initial displacements in a 600-degree of freedom finite element problem. This problem became numerically unstable when a trial case was run with XFAC = 2.0.

TABLE III-1
Effect of Overrelaxation Factor
on Convergence

XFAC	1.3	1.4	1.5	1.6	1.7	1.8	1.9
Number of iterations	4360	3740	3000	2340	1740	1160	580

Note that, while in this case the convergence rate improves each time the overrelaxation factor is increased (except when we tried XFAC=2.0), this does not always happen. One problem with the Gauss-Seidel technique is that there is no way to determine the optimum value of the overrelaxation factor in advance. It must be done by trial and error.

Euler Extrapolation Scheme

VISCO employs an Euler extrapolation scheme (7) for the time integration of the equations for all three viscoplastic material models. During each timestep, the equations for the Bodner model are integrated as follows for each element (9):

$$z^i = z_1 - (z_1 - z_0) \exp[-mW_p^{i-1}] \quad (\text{III-7})$$

$$(D_2^P)^i = D_0^2 \exp[-\left(\frac{z_1}{3J_2^{i-1}}\right)^2 \frac{n+1}{n}] \quad (\text{III-8})$$

$$\{\dot{\epsilon}_{ij}^P\} = [(D_2^P)^i / J_2^{i-1}]^{1/2} \{S_{ij}\}^{i-1} \quad (\text{III-9})$$

$$\{d\epsilon_{ij}^P\} = \{\dot{\epsilon}_{ij}^P\} dt^i \quad (\text{III-10})$$

$$\dot{z}_{rec}^i = -A \left(\frac{z^i - z_2}{z_1} \right)^r z_1 \quad (\text{III-11})$$

$$W_p^i = W_p^{i-1} + \{S_{ij}\}^{i-1} \{dt_{ij}^P\} + \dot{z}_{rec}^i dt^i / [m(z_1 - z^i)] \quad (\text{III-12})$$

where the superscript i refers to the timestep. The accuracy of this time stepping algorithm is strongly influenced by the approximate integrations in Eqs (III-10) and (III-12) (7).

Solution Procedure

Unlike a linear elastic analysis where the coefficients of the stiffness matrix remain constant, the coefficients for a plasticity problem vary as a function of the load. Thus, elastic-plastic displacements are usually found by applying the load in small increments and correcting for changes in material properties after each increment. Small displacement plasticity problems are generally solved by one of two techniques (8). In the first, called the tangent modulus procedure, the effects of plasticity are accounted for directly in the stiffness matrix. The second technique,

called the residual force method, uses the elastic stiffness matrix during the entire analysis and treats plasticity as an applied load that is used in conjunction with the applied mechanical and thermal loads for general equilibrium. This is the technique employed in the VISCO finite element program.

The residual force method uses the following matrix relation:

$$[K]\{U\}^i = \{P\}^i + \{Q\}^{i-1} \quad (\text{III-13})$$

where $[K]$ is the plastic stiffness matrix, $\{U\}^i$ are the nodal displacements for the i^{th} timestep, $\{P\}^i$ is the applied load vector during the i^{th} timestep, and $\{Q\}^{i-1}$ is the effective plastic load vector computed from plastic strains accumulated prior to the i^{th} timestep. The algorithm for a typical timestep employing the residual force method proceeds as follows (9):

1. compute the current time

$$t = dt^i + t^{i-1}$$

2. compute the plastic strain rate

$$\{\dot{\epsilon}_{ij}^P\} = [(D_2^P)^i / J_2^{i-1}]^{1/2} \{S_{ij}\}^{i-1}$$

(this applies to the Bodner model only)

3. compute the approximate increment in plastic strain

$$\{d\epsilon_{ij}^P\}^i = \{\dot{\epsilon}_{ij}^P\} dt^i$$

4. compute the effective plastic load vector

$$\{Q\}^{i-1} = \int_{VOL} [B][D]\{\epsilon_{ij}^P\}^i dVOL$$

(see the Appendix for a description of the B and D matrices)

5. if the external loads are changing, compute the current external load vector

$$\{P\}^i = \dot{\{P\}}^i dt^i + \{P\}^{i-1}$$

6. compute the nodal displacements for Eq (III-13) using the Gauss-Seidel iterative technique
7. compute the total strain for the strain displacement relationships (Appendix)

$$\{\epsilon_{ij}\}^i = [B]\{U\}^i$$

8. compute the current stress as follows:

$$\{\sigma_{ij}\}^i = [D][\{\epsilon_{ij}\}^i - \{\epsilon_{ij}^P\}^i]$$

Since we are using the offset plastic strain discussed in section II, the stress depends only on the elastic strains.

9. check the timestep size by comparing the percent change in effective stress and effective strain during the current timestep to preselected stress and strain tolerances. If these tolerances are exceeded, the timestep size is reduced as discussed in the following section, and steps 1-9 are repeated for the same timestep. Otherwise, the program will either increase the timestep or leave it the same. A full discussion of the stress and strain tolerances may be found in reference (9).

10. Repeat the above process until reaching the desired simulation time.

Timestep Variation

VISCO is able to efficiently handle large changes in strain rates by varying the rate of which we step through time. Timesteps can vary from small fractions of a second for rapidly changing conditions, such as load application, to minutes or hours during steady state creep. After every iteration, the timestep size is updated so that we always use the largest timestep that the stress and strain tolerances will allow. This capability results in more efficient use of computer time than if the timestep sizes were fixed.

The amount of change in the timestep after any iteration is controlled by the parameters P_σ and P_ϵ . These parameters, which are a function of effective stress, effective strain, and the stress and strain tolerances, are defined as follows (9):

$$P_\sigma = \frac{\sigma_e^i - \sigma_e^{i-1}}{\sigma_e^{i-1} \sigma_{TOL}} \quad (III-14)$$

$$P_\epsilon = \frac{(d\epsilon_e^P)^i}{\epsilon_{TOTAL}^i \epsilon_{TOL}} \quad (III-15)$$

where the superscript i refers to the timestep and ϵ_{TOTAL} is the magnitude of a vector whose components are ϵ_x , ϵ_y and $0.5\gamma_{xy}$. Thus,

$$\epsilon_{TOTAL} = \sqrt{\epsilon_x^2 + \epsilon_y^2 + 0.5\gamma_{xy}^2}$$

P_σ and P_ϵ are evaluated for each element and a third parameter, P , is set equal to the largest one. The timestep size is then determined from the following equations:

$$\begin{aligned} dt^i &= 0.8dt^{i-1}/P && \text{if } P > 1 \\ dt^i &= dt^{i-1} && \text{if } 0.8 \leq P \leq 1 \\ dt^i &= 1.25dt^{i-1} && \text{if } 0.65 \leq P < 0.8 \\ dt^i &= 1.5dt^{i-1} && \text{if } P < 0.65 \end{aligned}$$

Finally, whenever a node is released to simulate crack growth, the timestep size, dt , is automatically set equal to the initial timestep size specified by the user.

The Yield Criterion

VISCO uses the von Mises yield criterion discussed in section II to determine when plastic flow begins. We obtain a linear elastic solution for all stresses, strains, and displacements until the first element yields or the total load is applied, whichever comes first. At this time, the viscoplastic material models are activated. Thus, even though the Bodner model is independent of a yield criterion, its implementation in VISCO makes it dependent on the von Mises yield criterion until after the first element yields or load application is complete. This was done so that the Malvern and Norton flow laws could be more easily incorporated in the program along with the Bodner model. It also results in a small savings in computer time.

IV. Experimental Procedure

The experimental data group used in this thesis was a subset of a larger group of data collected by Donath (24) for use in another project. Parts of his work specifically applicable to the specimens considered herein are summarized for reference.

Test Specimens

All test specimens were standard compact tension specimens such as that shown in Fig. IV-1. They will be referred to as specimen 7-1, 7-2, 7-3, and 7-4. The first number indicates the nominal thickness in 32nds of an inch, and the second distinguishes one specimen from another. Due to machining tolerances, the actual specimen thicknesses were slightly different from the nominal thicknesses shown above. Nominal stress intensity factors of 30, 35, 40 and 45 ksi-in^{1/2} (33.0, 38.5, 44.0, and 49.5 MPa-m^{1/2}) were considered.

The material used was IN-100, an advanced, nickel based superalloy used as a turbine disk material in the F-100 engine. At 1350 F (732 C), the modulus of elasticity of this material is 26,030,000 psi, and the initial yield stress is 130,000 psi.

The IN-100 was supplied in pancake form (Fig. IV-2) by its manufacturer, Pratt and Whitney Aircraft Group, United Technologies Corporation. The pancake was 1.5 inches (38mm) thick and 16 inches (405mm) in diameter. Specimens were

cut with their crack surfaces perpendicular to the flat surface of the pancake with some cracks pointing in the radial and some in the circumferential direction of the pancake. Donath determined that the crack plane orientation with respect to the pancake had no observable effect on crack growth for these specimens.

Specimens were cyclically loaded at room temperature in an MTS hydraulic servo-controlled testing machine for pre-cracking to a target total crack length of 0.65 inches (16.51mm) (24). After test termination, each specimen was pulled apart and the actual length of the fatigue induced starter crack was measured using the ASTM 3-point averaging method illustrated in Fig. IV-3.

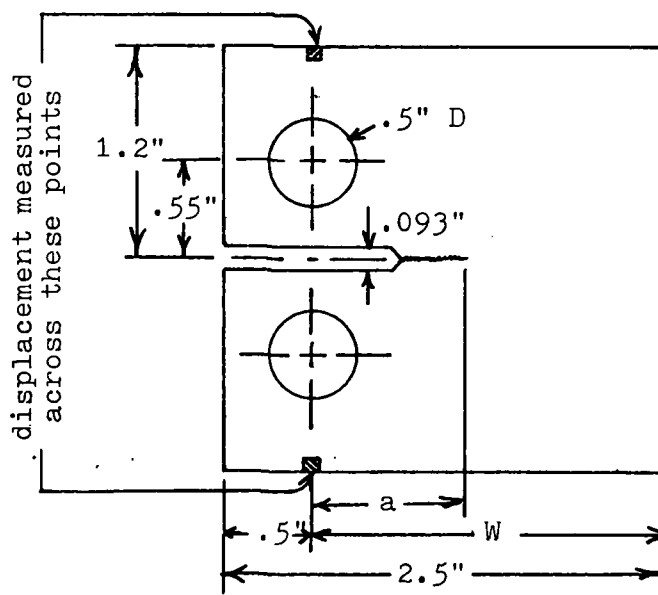


Fig IV-1. Standard Compact Tension Specimen



Fig IV-2. IN-100 Pancake Approximately 16 Inches
in Diameter and 1.5 Inches Thick

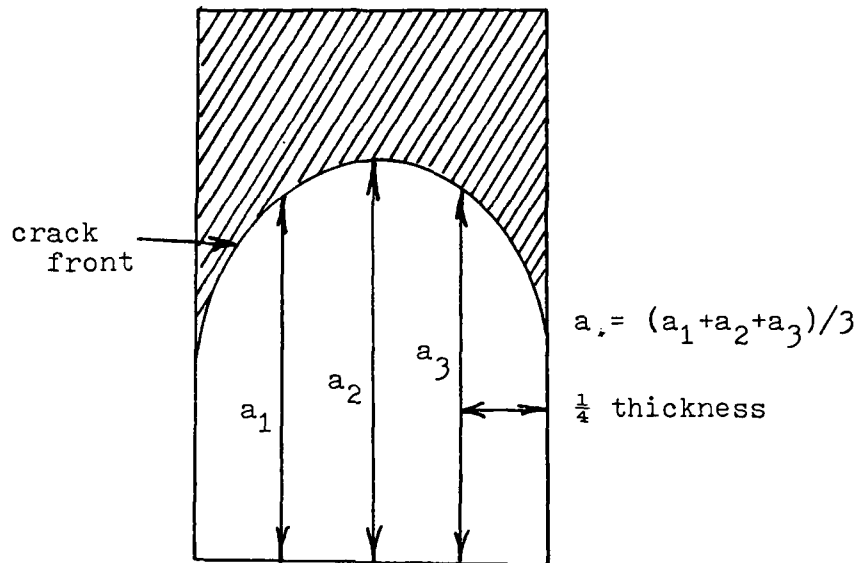


Fig IV-3. ASTM 3-Point Averaging Method for Crack Lengths

The loads used to produce the desired nominal stress intensity factors, K , were calculated using the initial surface crack lengths. However, surface crack lengths are not a good indication of the true crack length because of the characteristic thumbnail shape of most cracks. The crack front in the interior has often advanced quite a bit further than the surface crack measurements indicate. This effect is called tunneling. For later comparison with finite element models, the K values were recomputed using the actual initial crack lengths, "a". These values, along with other pertinent data for each specimen, are listed in Table IV-1. The equation used to calculate the K values in Table IV-1 was:

TABLE IV-1

Nominal Versus Actual K Values for
Compact Tension Specimens

Specimen No.	Load lb	Thickness in	Initial "a" in	Nominal K ksi $\sqrt{\text{in}}$	Actual K ksi $\sqrt{\text{in}}$
7-1	1762	.2134	.6617	35	36.4
7-2	1524	.2154	.6642	30	31.2
7-3	2034	.2154	.6637	40	41.7
7-4	2280	.2154	.6634	45	46.7

$$K_I = \frac{P}{B\sqrt{a}} f\left(\frac{a}{w}\right) \quad (\text{IV-1})$$

where K_I is the mode I stress intensity factor, P is the applied load, B is the specimen thickness, and a is the initial crack length. The $f\left(\frac{a}{w}\right)$ term is a geometry correction factor for the compact tension specimen and is given as (25):

$$f\left(\frac{a}{w}\right) = \left[29.60\left(\frac{a}{w}\right) - 185.5\left(\frac{a}{w}\right)^2 + 655.7\left(\frac{a}{w}\right)^3 - 1017\left(\frac{a}{w}\right)^4 + 638.9\left(\frac{a}{w}\right)^5 \right] \quad (\text{IV-2})$$

where w is the horizontal distance from the centerline of the loading pin holes to the far end of the specimen (see Fig. IV-1).

Apparatus and Instrumentation

Constant load was applied in a 10,000 lb (44.48 kN) capacity creep test frame having a 20 to 1 loading ratio (24). Specimens were surrounded by an oven with viewing ports on both sides and inside dimensions of 7x7x4 in (178x178x102 mm).

This oven maintained the temperature at 1350 F (732 C) for the duration of each test.

Displacements in the plane of load applications were measured across the ends of the specimen at a point directly above the loading pins (Fig. IV-1). Measurements were taken using a pair of linear variable transducers (LVDT) mounted below the oven and connected to the specimen through two E-shaped plates of IN-718 that were rigidly attached to the top and bottom of the specimen. This technique was first demonstrated by Mills, et al. (26). The LVDT's were bench calibrated and linear over a midrange of 0.150 inches (4mm).

V. Finite Element Models

Mesh Layout

Four different finite element meshes were used to test sensitivity of the models to changes in element size in the vicinity of the crack tip and in the area directly above the loading pin holes. These meshes (Figs. V-1 to V-4) will be referred to as mesh 1, 2, 3, and 4. Due to symmetry, only one half of the specimen geometry was modeled.

The element size reduction scheme and an expanded view of the element layout around the crack tip are shown in Fig. V-5. This region of uniform elements ahead of the initial crack tip avoids unrealistic changes in compliance, as the crack grows through the model, that can develop when non-uniform element sizes are used (9). The number of uniform elements near the crack tip and the degree of refinement represented a tradeoff between the anticipated amount of crack growth and the computer time required to carry out the simulation. Meshes 1 and 3 had 32 uniform elements with a height and base of 0.025 in (0.065cm), while meshes 2 and 4 had 24 uniform elements with a height and base of 3.125×10^{-3} in (7.9375×10^{-3} cm).

This general pattern of elements was used by Ohtani and Nakamura (27) for a center cracked plate. It permits an unlimited number of size reductions while also insuring that

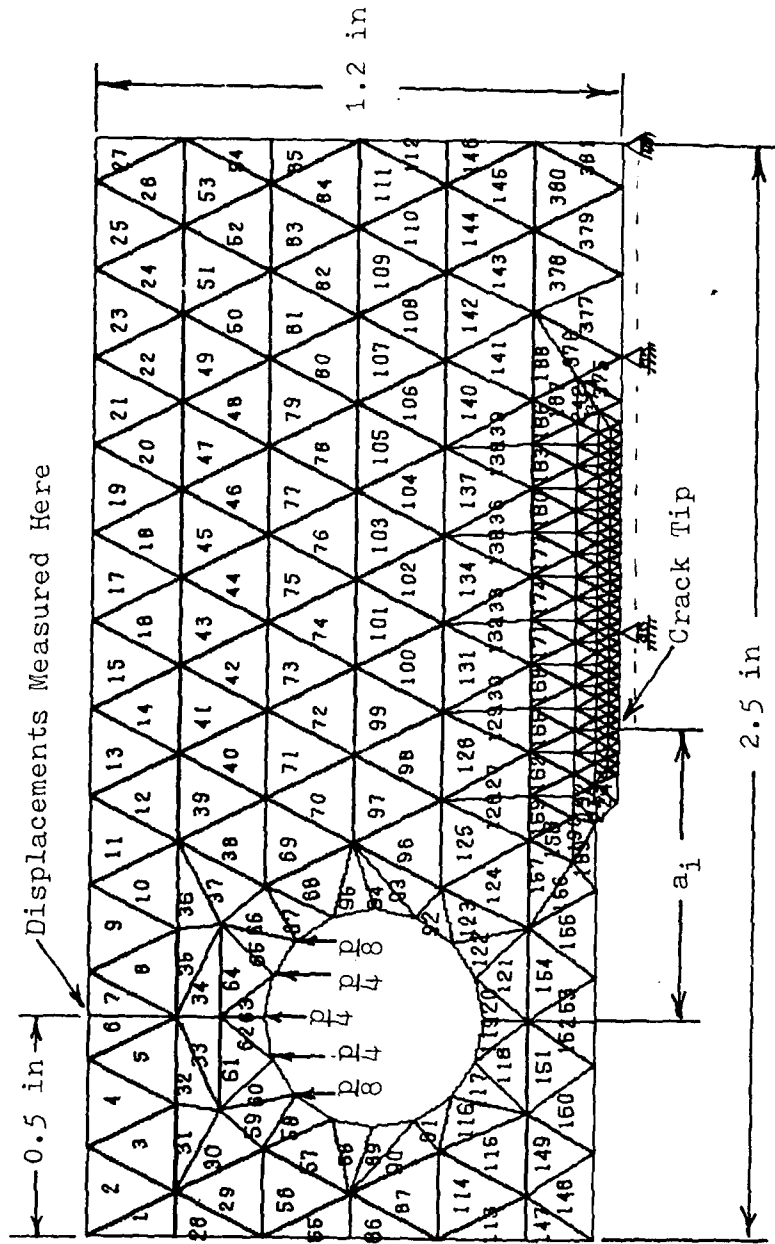


Fig. V-1. Finite Element, Constant Strain Model of the Compact Tension Specimen (Mesh 1)

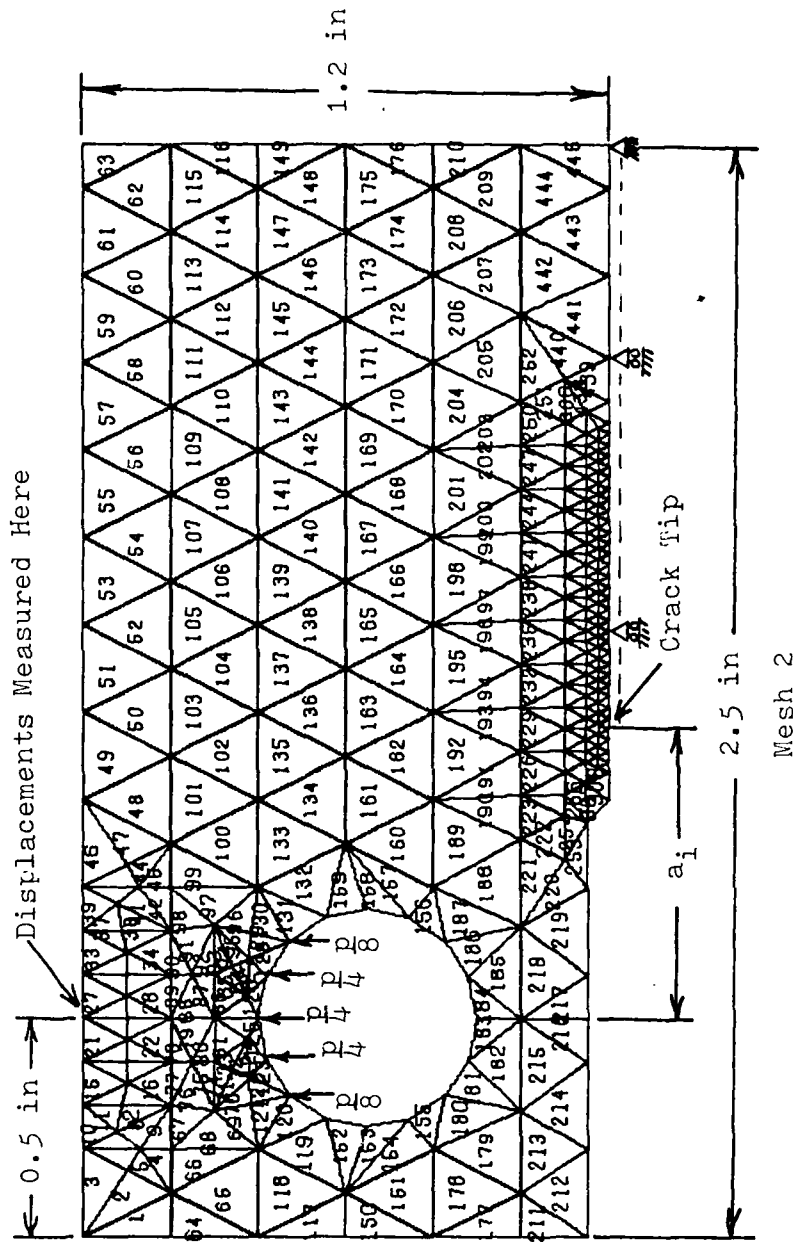


Fig. V-2. Finite Element, Constant Strain Model of the Compact Tension Specimen (Mesh 2)

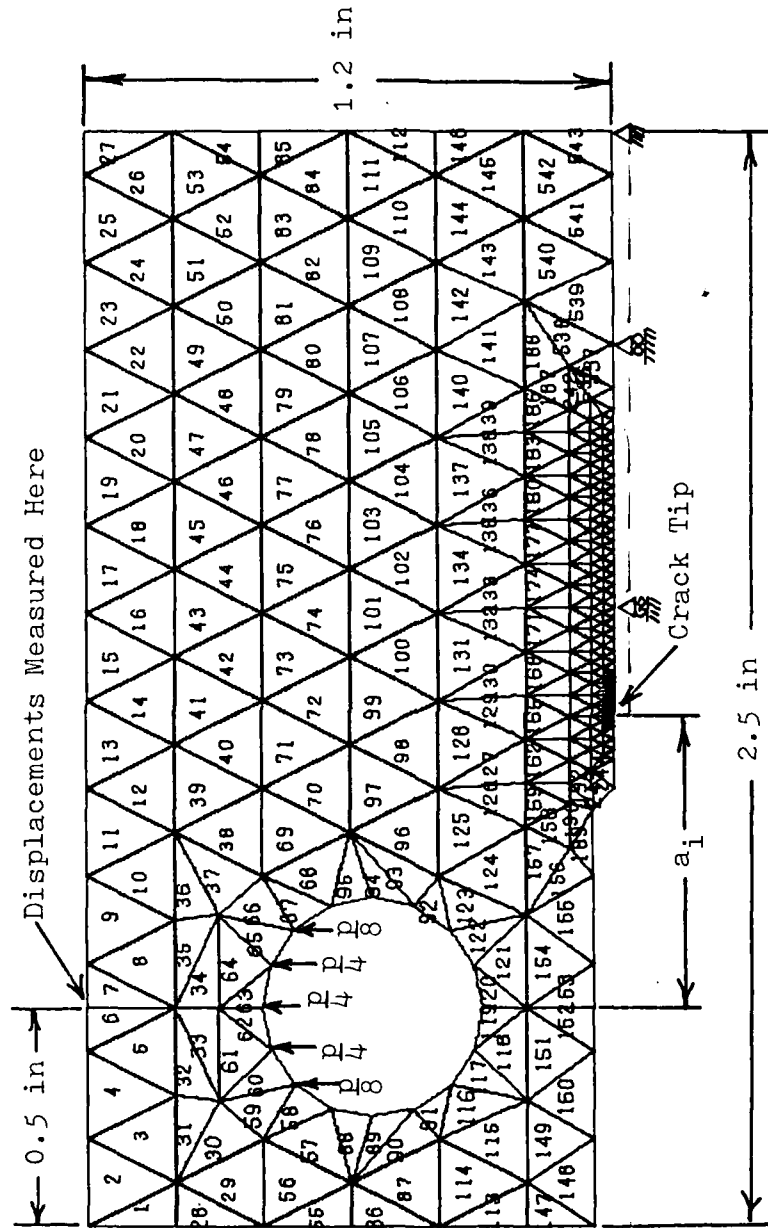


Fig. V-3. Finite Element, Constant Strain Model of the Compact Tension Specimen (Mesh 3)

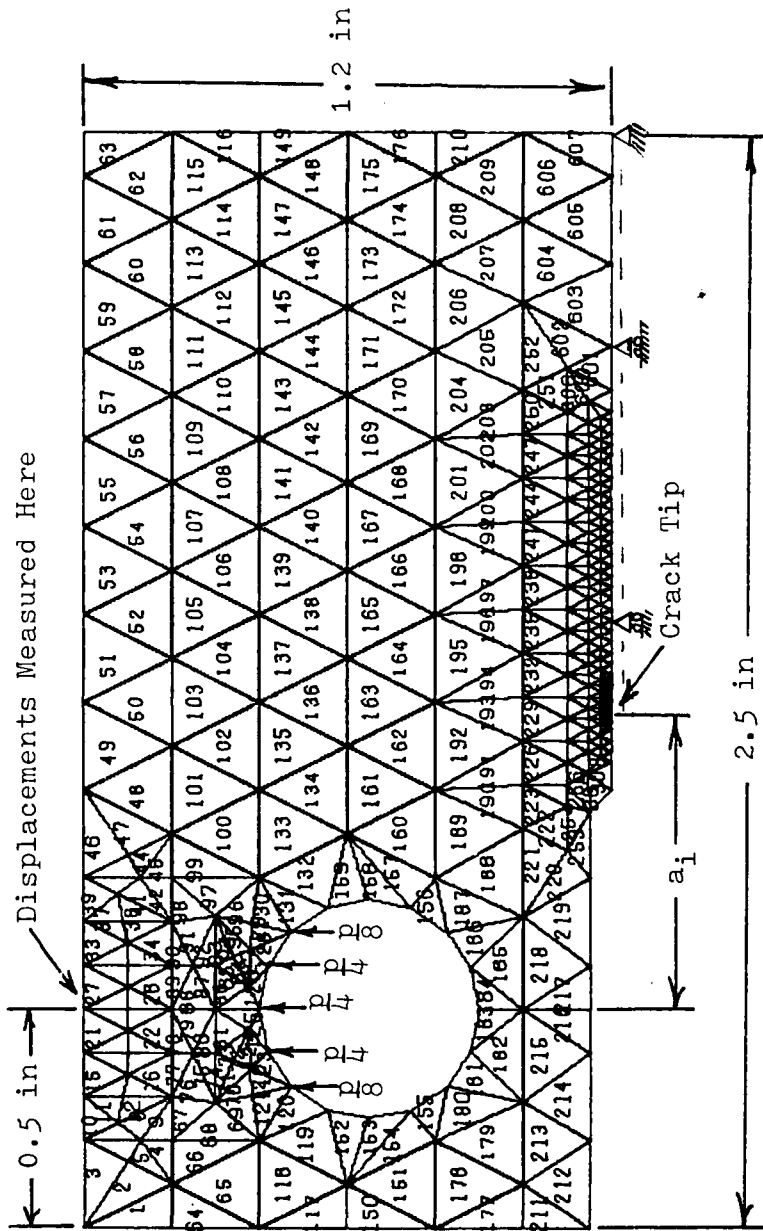


Fig. V-4. Finite Element, Constant Strain Model of the Compact Tension Specimen (Mesh 4)

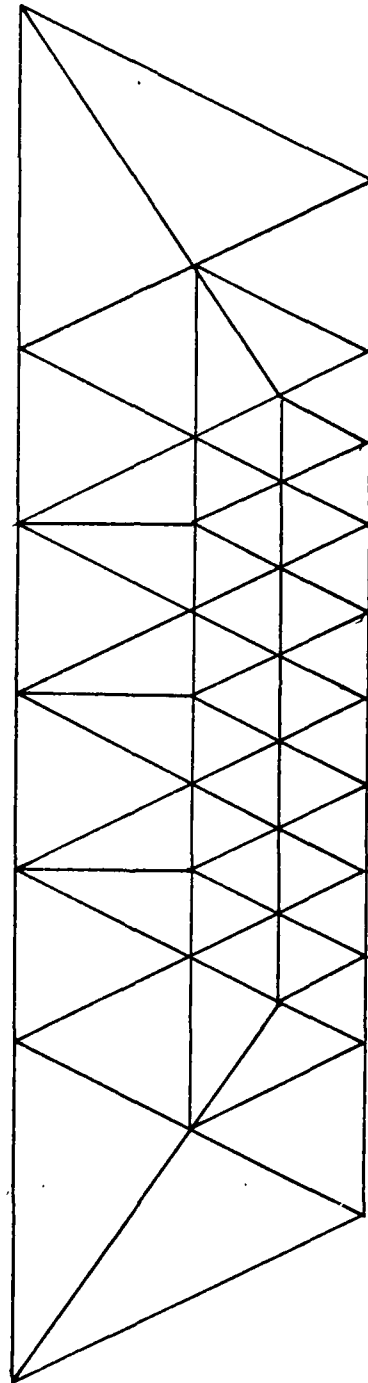


Fig. V-5. Uniform Mesh Ahead of Crack Tip

no two neighboring elements differ in size by more than a factor of 2. Fitting the elements around the loading pin holes required a change in element layout from that used in the rest of the specimen, but the maximum size differences between neighboring elements remains close to a factor of 2. Aspect ratios varied from 1.0 to 0.5 for the elements in the body of the specimen, while some elements around the loading pin holes had aspect ratios as high as 3.

Mesh 1 contains 381 elements and 234 nodes. The area of the largest elements is 0.02in^2 (0.129cm^2), while the elements in the vicinity of the crack tip have been refined to an area of $3.125 \times 10^{-4}\text{in}^2$ ($2.016 \times 10^{-3}\text{cm}^2$).

Since high stress gradients exist in the area of the specimen directly above the load, a refinement of the mesh in this region was tested to see what effect it had on the stress transmitted to the crack tip. This refinement was incorporated in mesh 2, which contained 445 elements and 267 nodes.

Mesh 3, which contained 543 elements and 327 nodes, was the same as mesh 1, except that the elements in the immediate vicinity of the crack tip were refined to an area of $4.8848 \times 10^{-6}\text{in}^2$ ($3.1494 \times 10^{-5}\text{cm}^2$).

Mesh 4, with 607 elements and 360 nodes, incorporates both the refinement above the load added in mesh 2 and the crack tip refinement added in mesh 3.

Comparison of Meshes

To test mesh accuracy, displacements generated by elastic VISCO runs with each of the four meshes subjected to an applied load of 2280 pounds were compared to displacements calculated using equations given in reference (28). For plane stress conditions, these equations are:

$$\delta_1 = \frac{P}{E} V_1 \left(\frac{a}{b} \right) \quad (V-1)$$

$$\delta_2 = \frac{P}{E} V_2 \left(\frac{a}{b} \right) \quad (V-2)$$

where δ_1 , δ_2 , a and b are defined in Fig. V-6 and values of V_1 and V_2 are obtained from Fig. V-7. Accuracies are expected to be 2 percent for V_1 and 1 percent for V_2 for $0.3 \leq a/b \leq 0.7$ (28). Results are given in Table V-1.

TABLE V-1
Comparison of Calculated and Finite
Element Model Displacements

	Calculated	Mesh 1	Mesh 2	Mesh 3	Mesh 4
δ_1 (in)	2.471 $\times 10^{-3}$	2.202 $\times 10^{-3}$	2.158 $\times 10^{-3}$	2.225 $\times 10^{-3}$	2.245 $\times 10^{-3}$
δ_2 (in)	1.471 $\times 10^{-3}$	1.348 $\times 10^{-3}$	1.308 $\times 10^{-3}$	1.366 $\times 10^{-3}$	1.366 $\times 10^{-3}$

The assumption that plane stress conditions prevail at the crack tip in these specimens is justified by research conducted by Atluri and Nakagaki (29). They showed that plane stress conditions best characterized the behavior of

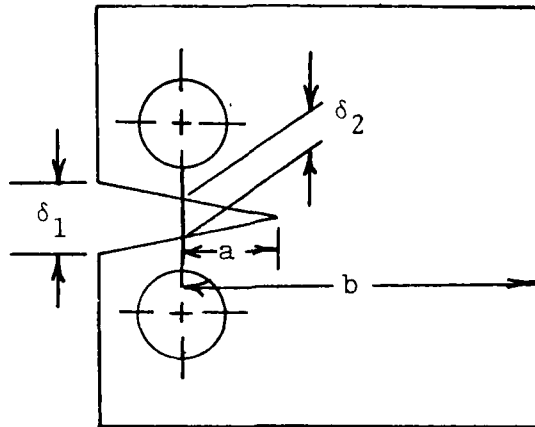


Fig. V-6. Definition of Terms for Use with Eqs. V-1 and V-2

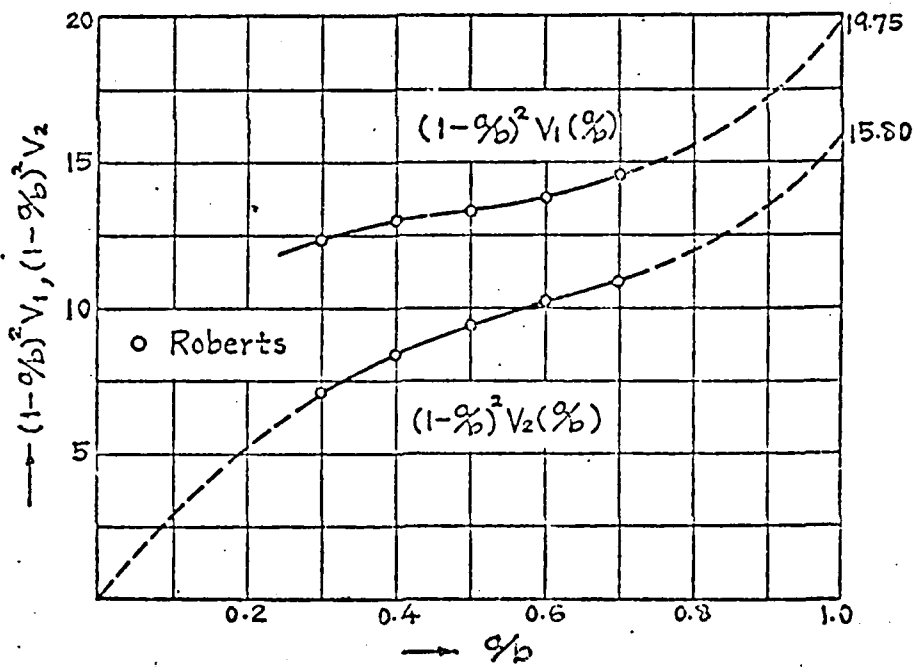


Fig. V-7. Crack Mouth Opening Parameters for the Standard Compact Tension Specimen (28)

compact tension specimens one inch thick, much thicker than those used here.

Note that while the refinement above the loading pin incorporated in mesh 2 results in about 2 percent less displacement for δ_1 and δ_2 than for mesh 1, this decrease is not consistent throughout the model. The displacements directly above the loading pin were about 4 percent greater for mesh 2 than for mesh 1.

As another check on the meshes, the stress intensity factors at the crack tip were estimated from the elastic VISCO runs by using a technique suggested in reference (30). If we consider the y component of stress, the stress intensity factor for a given element is calculated as follows (25):

$$K_I = \frac{\sigma_y (2\pi r)^{1/2}}{\cos \frac{\theta}{2} [1 + \sin \frac{\theta}{2} \sin \frac{3\theta}{2}]} \quad (V-3)$$

where r and θ are cylindrical coordinates that locate the centroid of the element relative to the crack tip.

The finite element procedure is inaccurate near the crack tip due to the inability of the elements to represent the stress singularity. Therefore, the stress intensity factor calculated with Eq (V-3) will not be accurate. However, a reliable estimate of the stress intensity factor at the crack tip can be obtained if we plot the calculated stress intensity factor, K, for several elements in the vicinity of the crack tip versus distance, r. If the exact stresses were used, the exact value of K would be at the

intercept of this curve with the axis at $r = 0$ (30). We can estimate K with the stresses from our finite element analysis by plotting calculated K values for increasing values of r until the resulting curve reaches a constant slope. The K value for the finite element mesh is obtained by extrapolating this slope back to $r = 0$. Results from elastic VISCO runs for each mesh using the applied load corresponding to specimen 7-4 are shown in Figs. V-8 to V-11 and in Table V-2.

TABLE V-2
Comparison of Actual and Finite Element
Mesh Stress Intensity Factors

Mesh	Actual K (ksi in ^{1/2})	Finite Element K (ksi in ^{1/2})	% Error
1	46.7	43.9	6.4
2	46.7	43.9	6.4
3	46.7	45.9	1.6
4	46.7	45.9	1.6

As a final comparison between meshes, computer runs were made to estimate the amount of crack growth in 40 minutes for specimen 7-4. The resulting estimates along with the computer time required for each run on the CDC 6600 computer are shown in Table V-3.

A review of the data presented in Tables V-1, V-2 and V-3 shows that the refinement above the loading pin hole incorporated in meshes 2 and 4 made almost no difference in the stress intensity factor at the crack tip. However, the

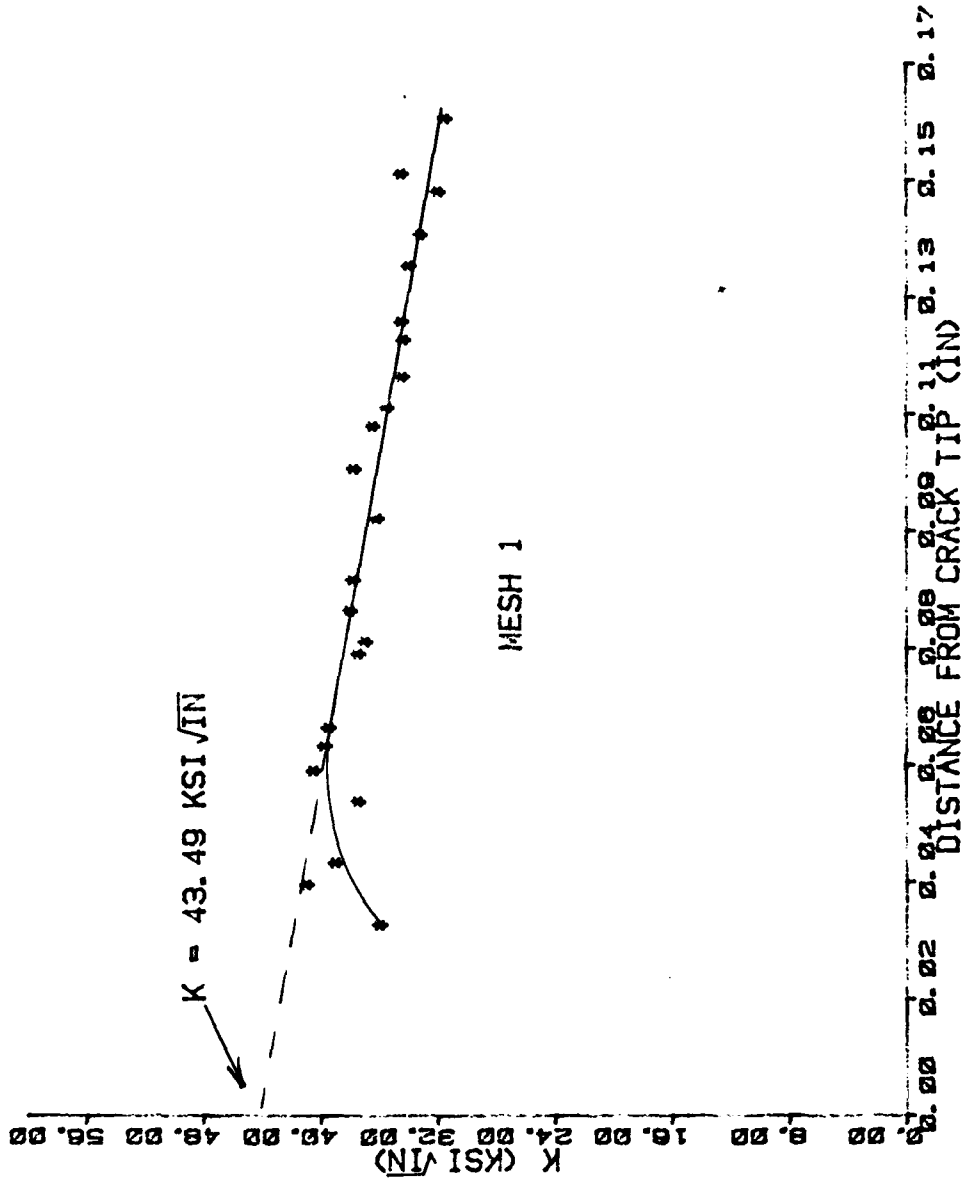


Fig. V-8. Finite Element Estimate of Stress Intensity Factor for Mesh 1 with an Applied Load of 2280 lbs.

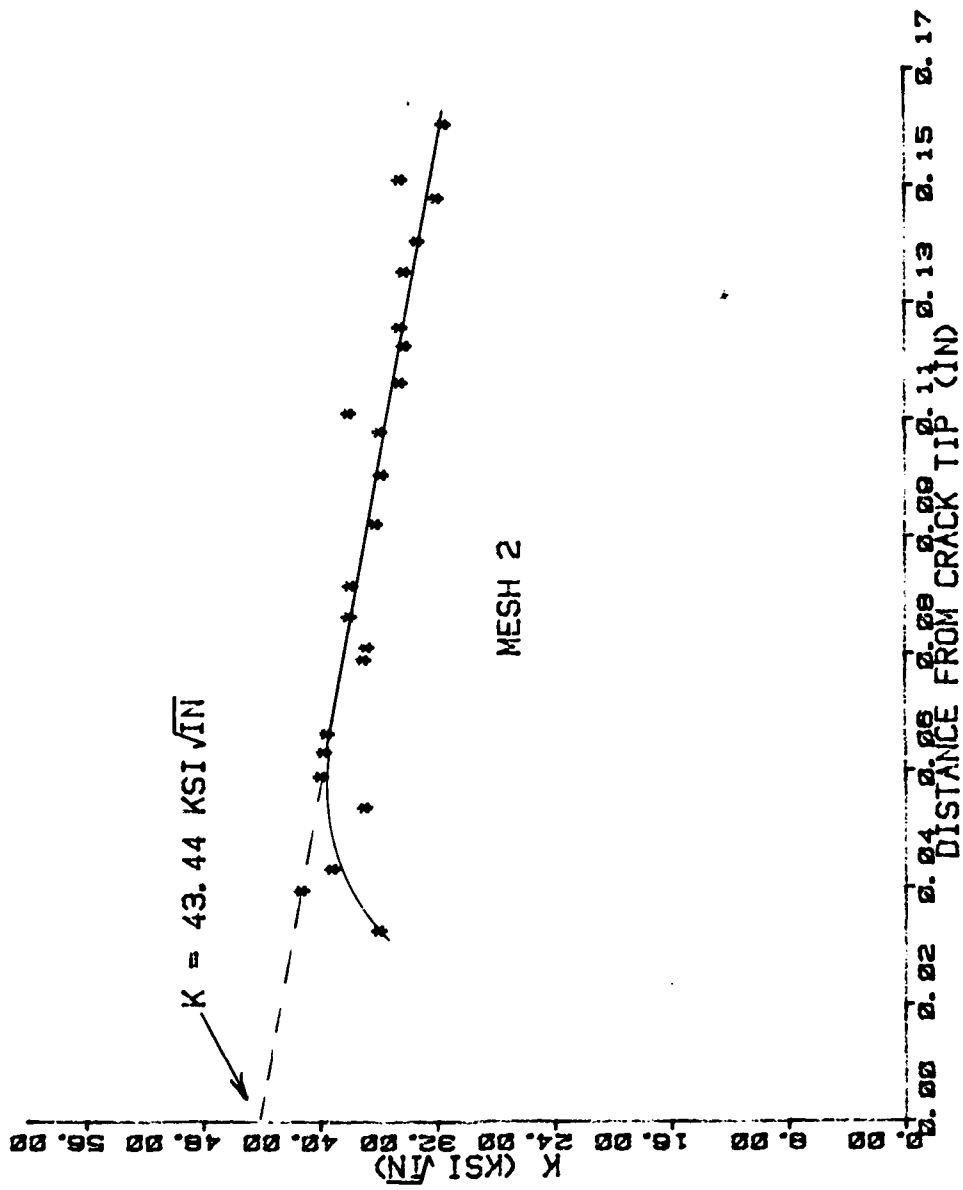


Fig. V-9. Finite Element Estimate of Stress Intensity Factor for Mesh 2 with an Applied Load of 2280 lbs.

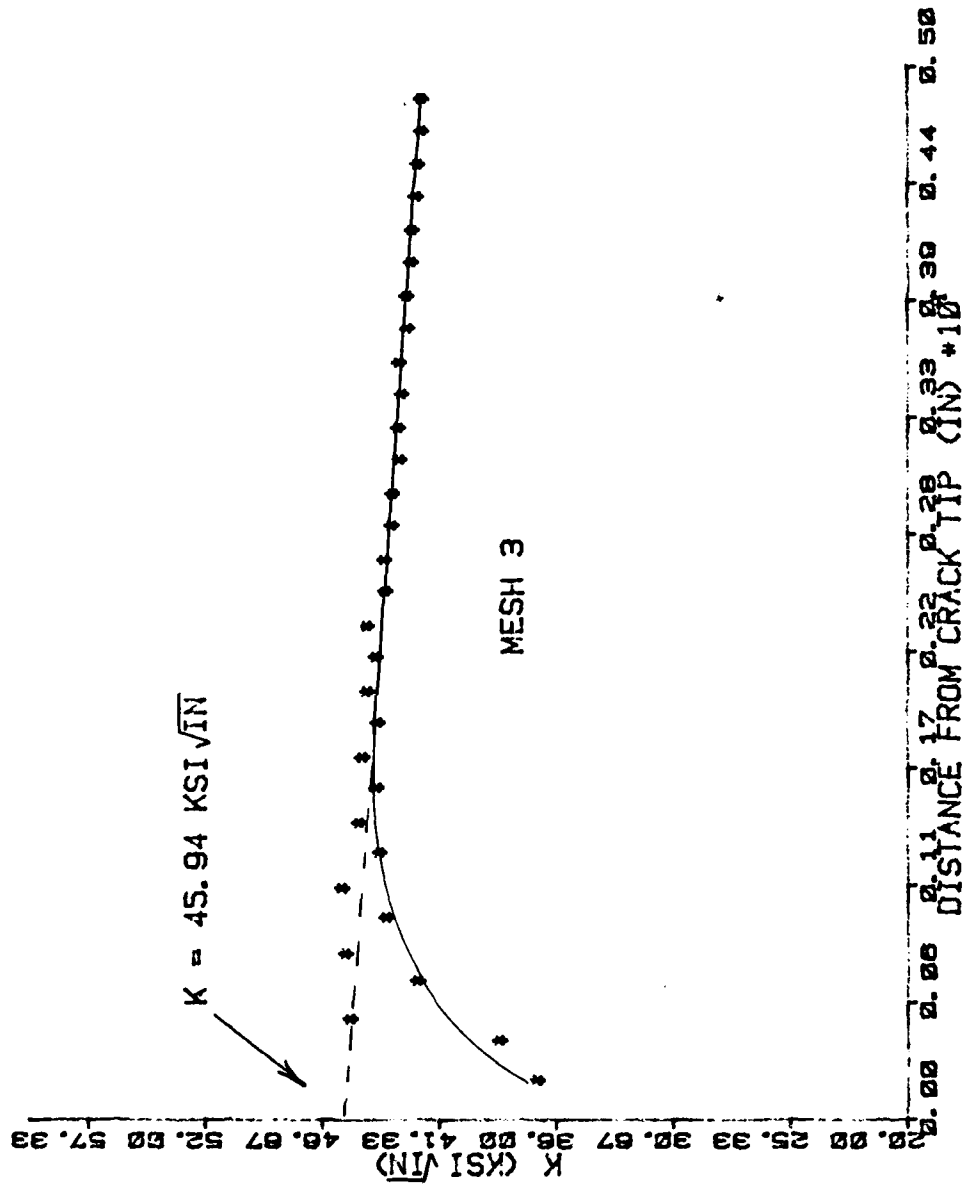


Fig. V-10. Finite Element Estimate of Stress Intensity Factor for Mesh 3 with an Applied Load of 2280 lbs.

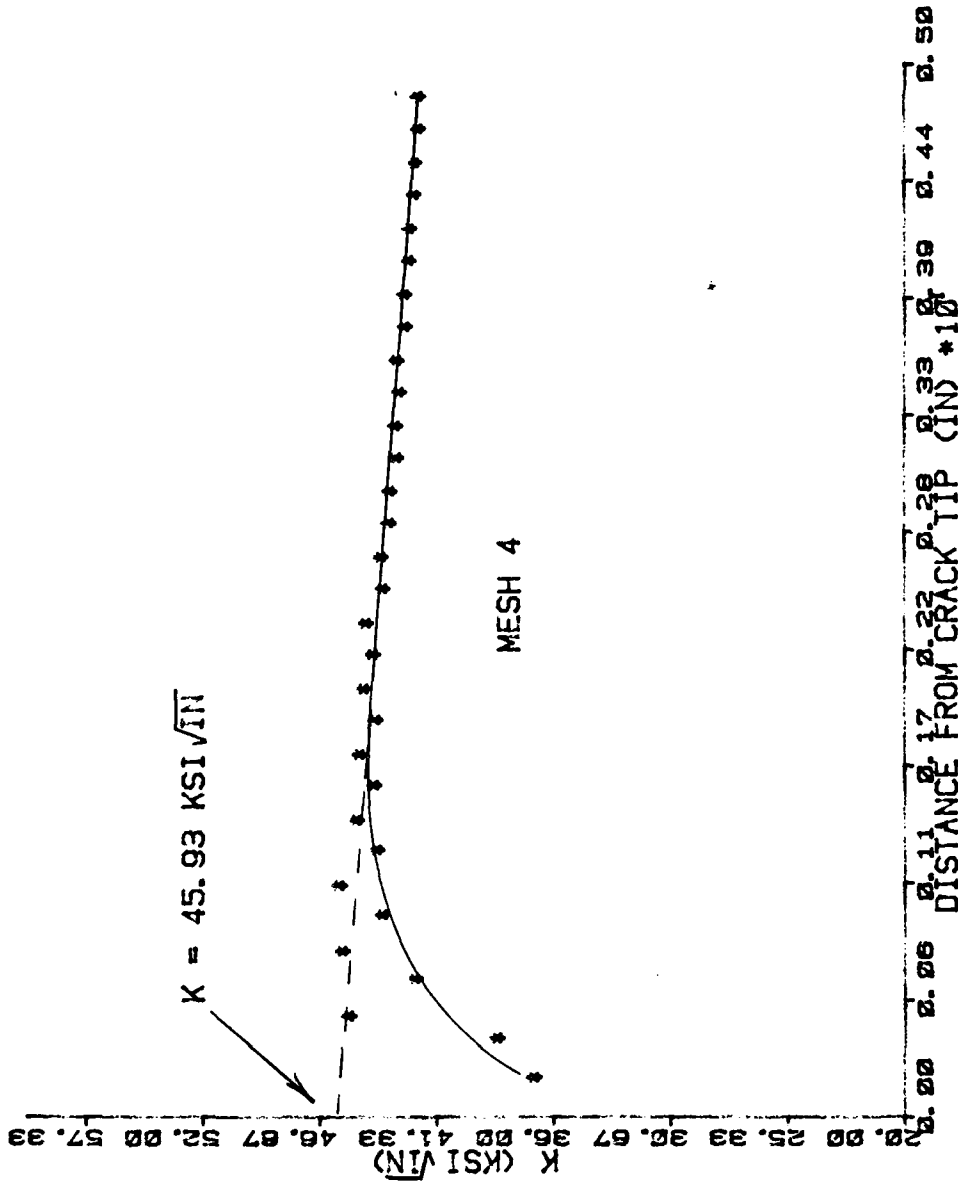


Fig V-11. Finite Element Estimate of Stress Intensity Factor for Mesh 4 with an Applied Load of 2280 lbs.

TABLE V-3

Estimated Crack Growth After 40 Minutes
for Specimen 7-4

Mesh	Central Processor Time (sec)	Estimated Crack Growth (in)
1	344	.0529
2	599	.0577
3	2360	.0492
4	3217	.0501

refinement of the crack tip elements in meshes 3 and 4 improved the stress intensity factor estimates by about 5 percent. Additionally, while the displacement and crack growth estimates for meshes 1, 3 and 4 all tended to cluster about the same value, the results from mesh 2 deviated slightly from the rest of the group. It should also be noted that meshes 3 and 4 produced nearly identical results, but that mesh 3 required considerably less computer time to run than did mesh 4. After considering all of the preceding mesh comparisons, it was decided that the refinement above the load incorporated in meshes 2 and 4 was ineffective and that all further computer runs would be made using meshes 1 and 3.

As shown in Table V-3, the crack growth estimate from mesh 1 differed only 7 percent from that given by mesh 3, while mesh 3 used almost 700 percent more computer time. However, mesh 3 did a much better job in displaying the stress

and strain fields near the crack tip because the larger elements used in mesh 1 tended to smear out the rapid changes occurring in this area. For these reasons, mesh 1 was used to test the feasibility of using far-field displacement measurements to predict crack growth over periods of several hours where the computer time required to run mesh 3 would have been prohibitive. Mesh 3 was used for short runs (40 minutes) and for studying the behavior near the crack tip.

Based on good agreement between actual and finite element mesh K values as well as between model displacements and those calculated using Eq (V-1) and (V-2), it was assumed that meshes 1 and 3 adequately modeled the test specimens.

Effective Crack Lengths

As previously mentioned, surface crack lengths are not a good indication of actual crack length. In addition, accurate measurement of surface crack lengths is difficult in the high temperature environment studied here because oxidation on the surface of the specimen tends to mask the crack. Even with accurate surface crack measurements, there is no way to determine how long the crack actually is at any specific time during the test because we do not know how much tunneling is taking place. For this reason, the concept of an effective crack length determined from specimen compliance measurements is introduced as a measure of crack length for severely tunneled crack front geometries. Donath showed that the effective crack length, a_{eff} , can be determined from

the following equation:

$$E \cdot B \cdot C = 1 + m\alpha^n \quad (V-4)$$

where $\alpha = a_{\text{eff}}/w$ (see Fig. IV-1), E is an effective modulus of elasticity determined from compliance measurements at the start of the test (24), and C is the compliance (slope of a load versus displacement curve). The coefficients in Eq (V-4) are given by Donath as:

$$\begin{aligned} l &= 11.51 \\ m &= 248.8 & 0.25 \leq \alpha \leq 0.5 \\ n &= 3.167 \\ l &= 22.468 \\ m &= 632.7 & \alpha > 0.5 \\ n &= 5.240 \end{aligned} \quad (V-5)$$

As the crack grows through the specimen, the newly exposed surfaces will become heat tinted. Thus, if a specimen is not taken all the way to failure, the final crack length can be determined by breaking it open and measuring the tinted crack front. These final crack lengths agreed very well with the final effective crack lengths lending confidence to the effective crack length as a valid measure of crack growth (24).

The Hybrid Experimental-Numerical Technique

A hybrid experimental-numerical technique (HEN) was used with the finite element method to model crack growth in

the test specimens. As shown in Figs. V-12 through V-15, experimental displacement versus time plots for each specimen were approximated by linear fits to the data points. The equations of these lines were read into the computer program and used as crack growth criteria in the finite element models for simulation times of 40 minutes or less. For longer runs, smoothed displacement versus time plots given in reference (24) were used as the crack growth criteria. To provide a common starting point, both model and experimental displacements were set equal to zero after load application was complete. (Note that displacements given in Figs. V-12 through V-15 do not include load application displacements.) Thereafter, any increase in experimental displacements over the model displacements was attributed to crack growth in the test specimens. At this time, fixed nodes in the model were released to simulate crack growth and bring the displacements back into line. This procedure was repeated each time the model displacements became less than the experimental displacements until the desired simulation time was reached.

Crack Tip Node Release Method

The first step in releasing a crack tip node is to calculate the total force on that node. This force is calculated from the stresses in the adjacent element as follows:

$$\{f\} = \sum_{\text{adjacent elements}} \int_{\text{VOL}} [B] \{\sigma_{ij}\} d_{\text{vol}} \quad (V-6)$$

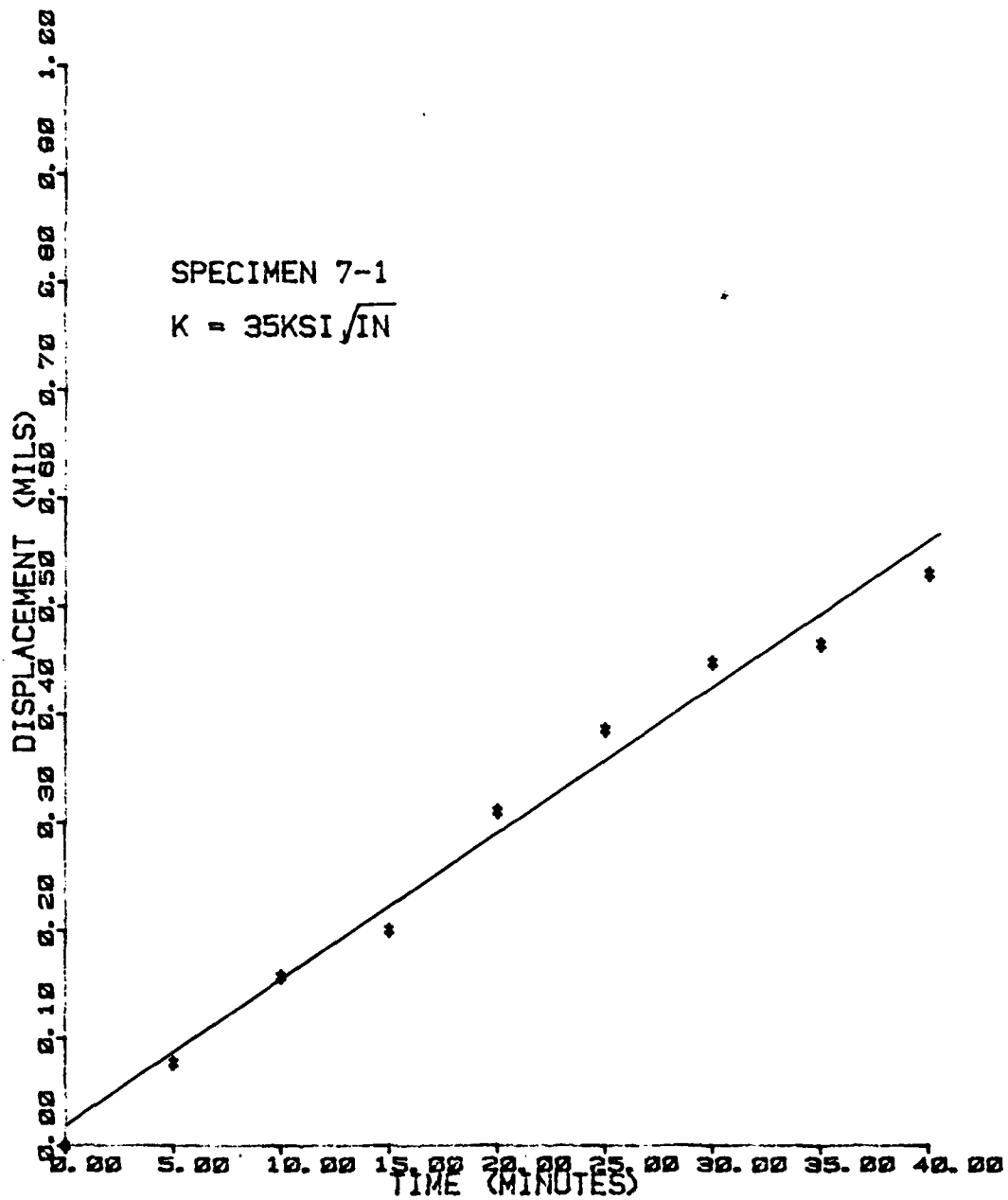


Fig. V-12. Load Line Displacement as a Function of Time for Specimen 7-1

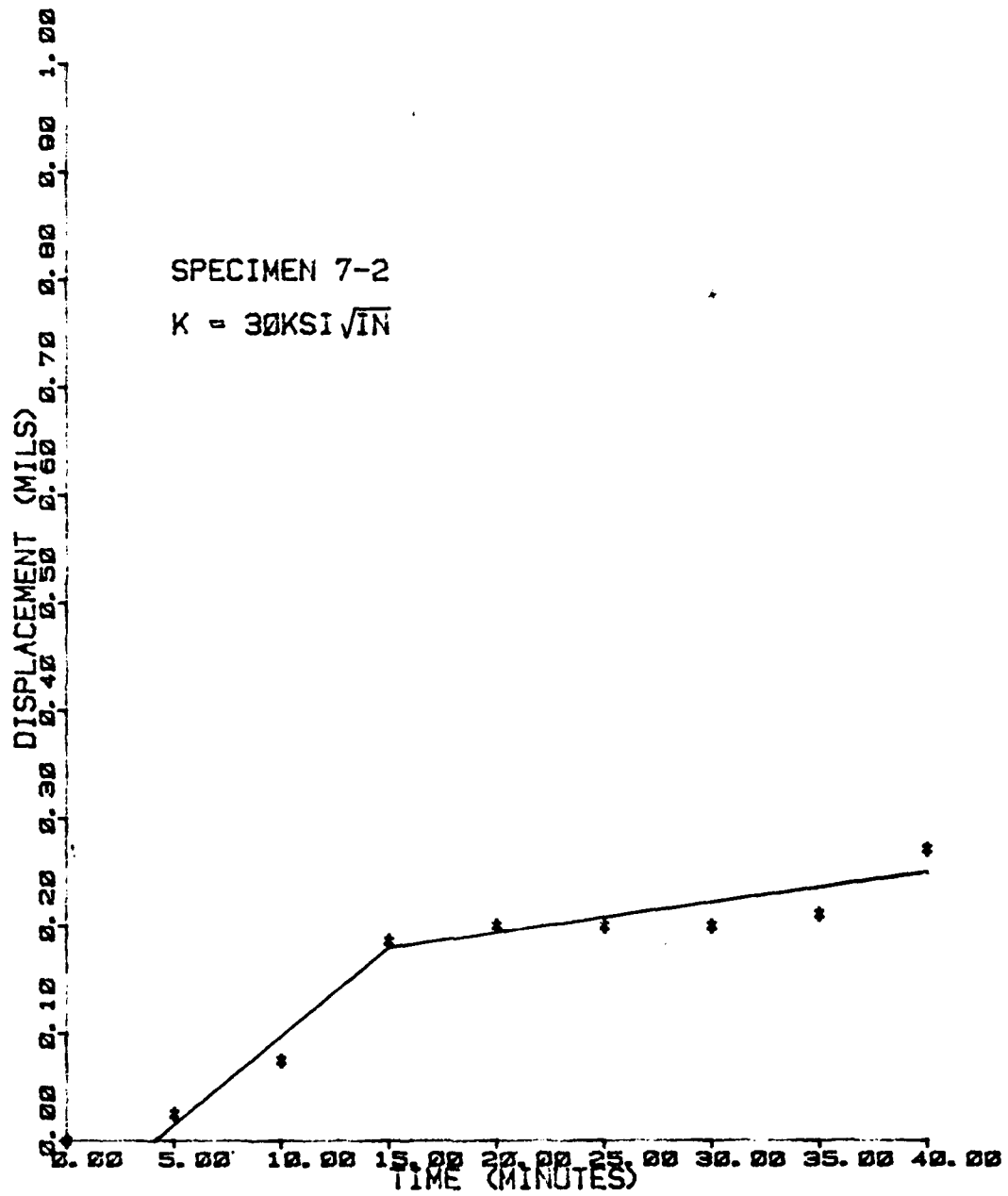


Fig. V-13. Load Line Displacement as a Function of Time for Specimen 7-2

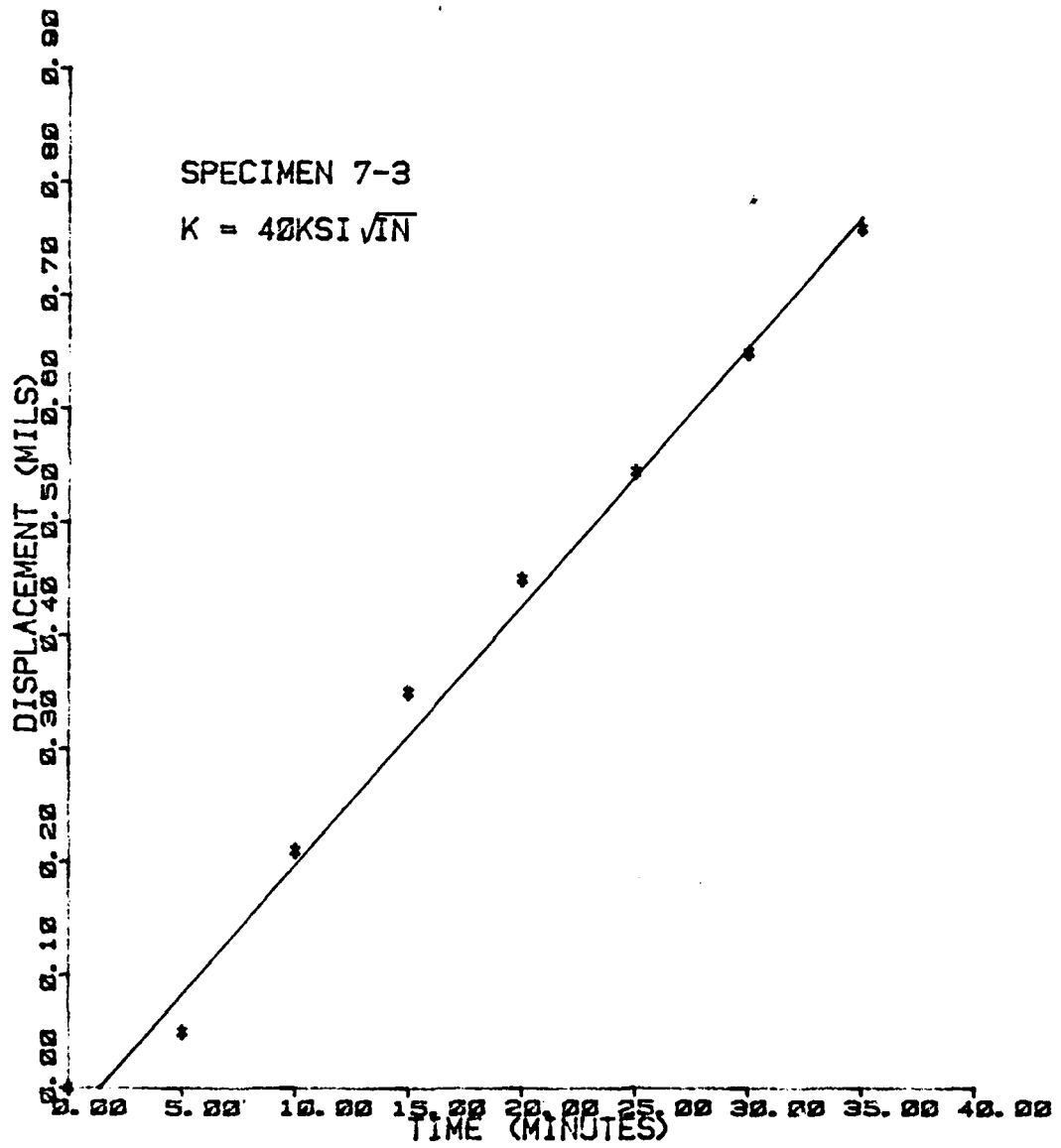


Fig. V-14. Load Line Displacement as a Function of Time for Specimen 7-3

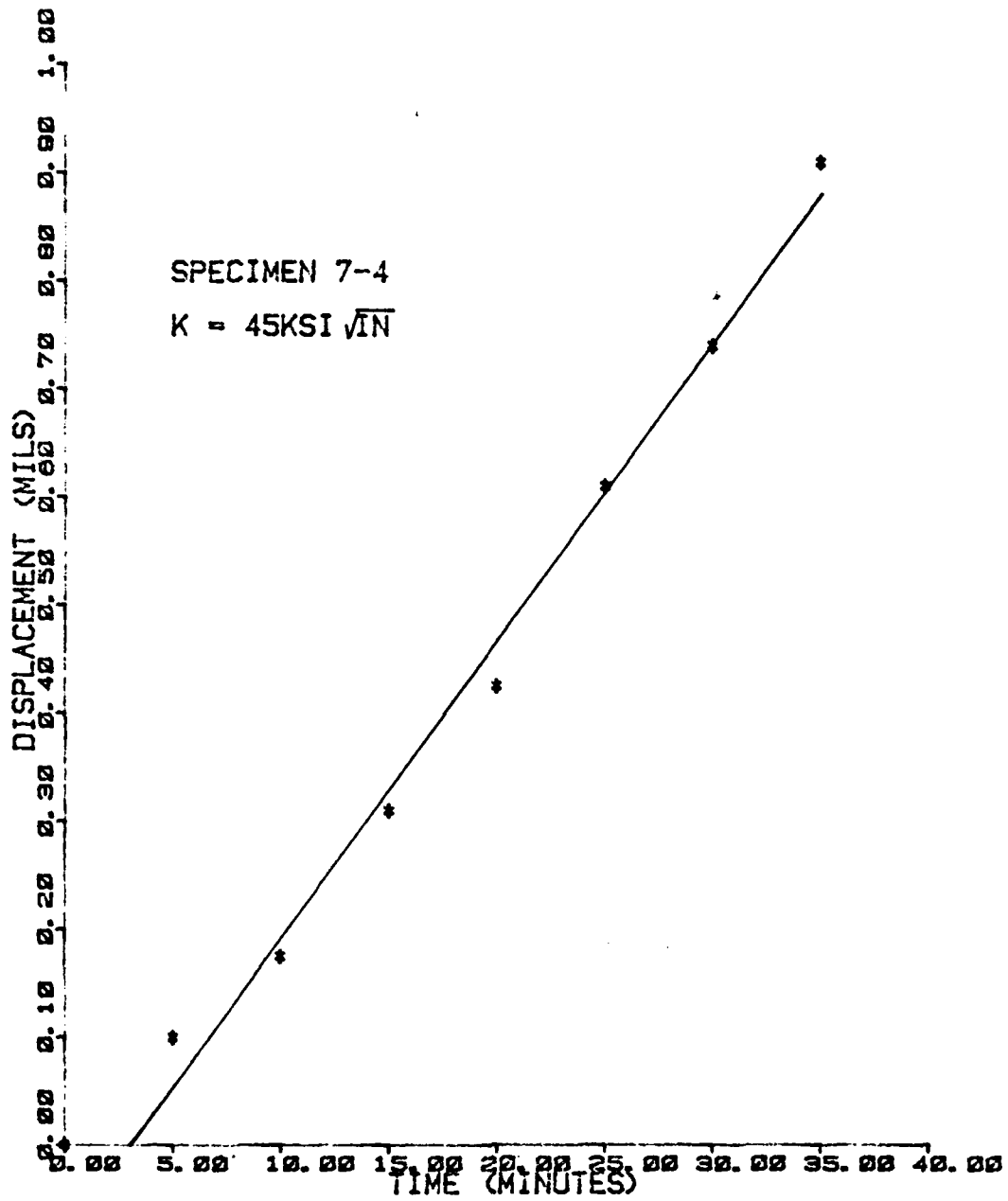


Fig. V-15. Load Line Displacement as a Function of Time for Specimen 7-4

The node restraining force is set equal to the component of f perpendicular to the crack line, f_y . Next, we convert the boundary condition on the node from zero y displacement to an applied force, f_y . This force is then removed over a set period of time based on the maximum anticipated crack growth rate and the size of the elements the crack is growing through (i.e., maximum crack growth rate equals element size divided by release time). Since Hinnerichs (9) showed that the node release time had little effect on results, the same release time was used for all four specimens and only variations due to mesh changes were considered. Nodes in mesh 1 were released in 100 seconds, while those in mesh 3 were released in 40 seconds.

The change from a displacement to a force boundary condition at the crack tip node being released is easily handled by the Gauss-Seidel iterative solution technique discussed in section III. During iterations, the equilibrium equations for fixed nodes are skipped. After a node is released, its equilibrium equations are included in all subsequent iterative solutions. No costly changes are required.

VI. Results and Discussion

The simultaneous use of experimental data from crack growth tests and a theoretical model of the cracked specimen was termed the Hybrid Experimental-Numerical Technique (HEN) by Kobayashi (31). Use of the HEN technique to predict crack growth in IN-100 was previously investigated by Hinnerichs (9). He showed that it could provide accurate estimates for small increments of creep crack growth in center cracked plates over short time periods (15 to 60 minutes). By using extremely accurate, near field (close to the crack) displacement measurements and a finite element mesh with crack tip elements that were roughly equal to the grain size of IN-100, he was able to predict creep crack growth to within 10 percent of post test measurements. Displacement readings were taken with a laser interferometer able to resolve movements as small as 0.004 mils (0.1 microns). This accuracy was considered essential since total crack growth in his tests was only about 4 mils (100 microns), making changes in displacements behind the crack quite small.

In contrast, the LVDT's used to measure displacements in this effort are accurate to about ± 0.5 mils. However, the compact tension specimens used here were subjected to higher stress intensity factors over longer experimental test

times than Hinnerichs' center cracked plates. Displacement changes of more than 20 mils were recorded in each test. Since the laser interferometer loses much of its sensitivity when displacements become much greater than 0.04 mils (1 micron), the accuracy lost by using LVDT's is not as great as it may seem at first glance. LVDT's have the advantage of being simple to use and much less expensive than a laser interferometer.

Another contrast between this effort and that of Hinnerichs is that, due to the combination of higher stresses and longer test times, the total crack growth herein was much larger. If crack tip elements as small as Hinnerichs' had been used, it would have been necessary to pop hundreds of nodes to model the total crack growth in these tests. As a compromise, two different meshes were incorporated--a fairly fine mesh for short runs and a coarser mesh for long runs.

Since the bulk of the computer time required to run the VISCO program is used by the node popping routine, elements were sized so that the amount of crack growth expected in any one run would not require more than 20 nodes to be released. This figure was chosen based on previous experience with the program that indicated that popping 20 nodes would take about 4000 seconds of central processor time on the CDC 6600 computer. It was felt that runs longer than this would not be an efficient use of computer time unless they were the only way to obtain accurate results. As it turned out, this method for sizing elements worked well

and use of finer meshes was not necessary.

As discussed in section V, the meshes used to carry out the analysis in this effort will be referred to as mesh 1 and mesh 3. The crack tip elements in mesh 1 were 32 times larger than Hinnerichs', while those in mesh 3 were 4 times larger. The coarseness of mesh 1 allowed the simulation of tests as long as 14 hours for the lower load cases, while remaining below the 4000 second limit we set for computer runs. It was not believed that the coarse mesh would provide anything better than gross estimates of creep crack growth, but the results turned out to be much better than expected.

Crack Growth Estimates

Table VI-1 shows the results of VISCO runs with meshes 1 and 3 after 40 minutes of simulated crack growth. Plots of crack growth versus time for the runs with mesh 3 are given in Figs. VI-1 through VI-4. Results from mesh 1 were not plotted because only two or three nodes were released during these runs. The average difference between the crack growth estimates from mesh 1 and mesh 3 was only 12 percent. Considering the fact that the crack tip elements in mesh 1 were 8 times larger than in mesh 3, the result was a surprise. However, even though mesh 1 is very coarse when compared to the mesh used by Hinnerichs, the area of the crack tip elements is still only $3.125 \times 10^{-4} \text{ in}^2$. Evidently, further refinement of the mesh from that used in mesh 1 results in very slow convergence as far as crack growth estimates

TABLE VI-1
 Crack Growth Estimates After 40 Minutes for
 Compact Tension Specimens

Specimen	K ksi/√in	Mesh 1 (coarse)	Mesh 3 (fine)	Donath's Effective Growth	Incubation Time (sec)	Av. Growth Rate (in/hr)
7-1	35	.0420	.0373	.0203	322	.06247
7-2	30	.0184	.0148	.0078	499	.02915
7-3	40	.0510	.0481	.0303	473	.09348
7-4	45	.0485	.0451	.0286	689	.09985

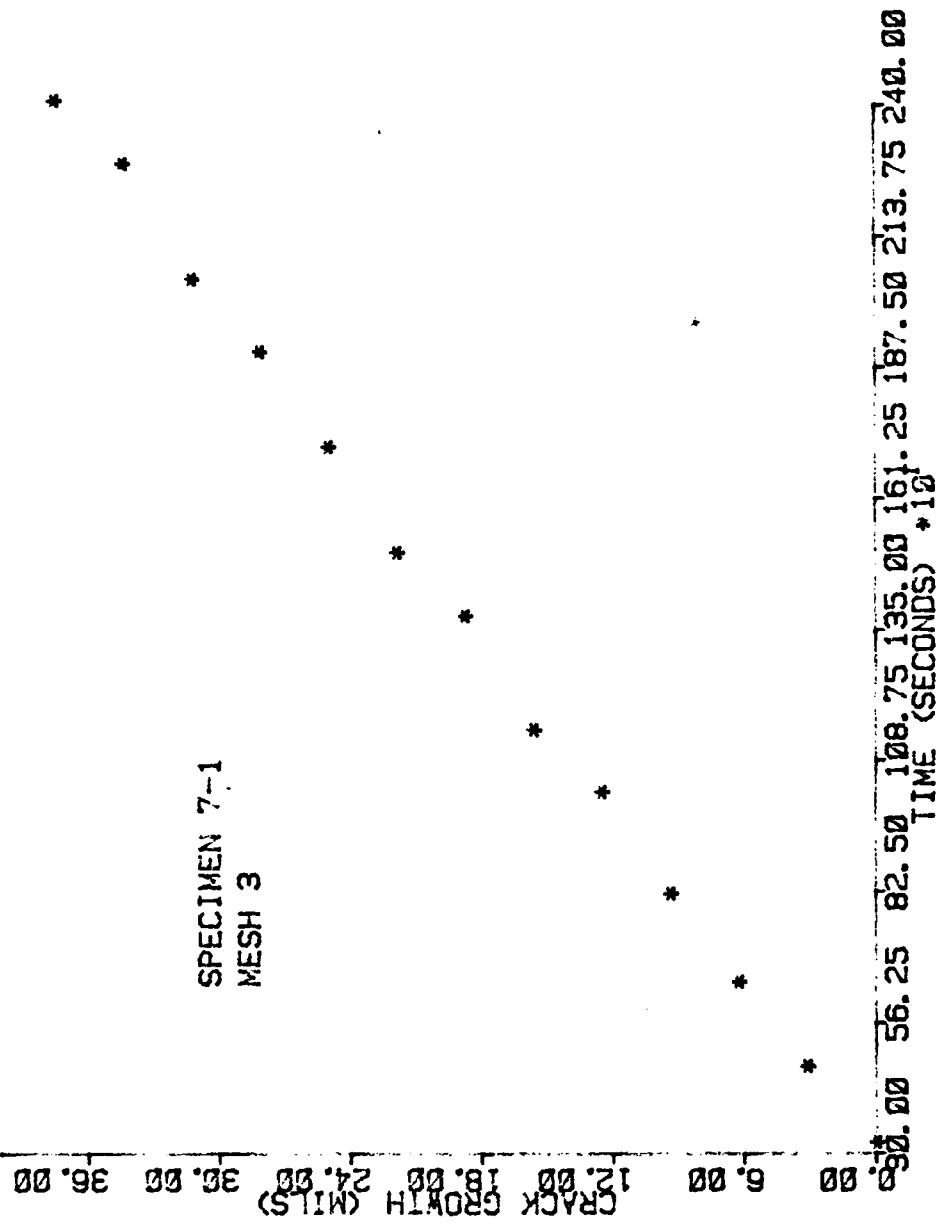


Fig. VI-1. Crack Growth as a Function of Time for Specimen 7-1

SPECIMEN 7-2
MESH 3

CRACK GROWTH (MILS)
 16.20 13.50 10.80 8.10 5.40 2.70 00

40.00 62.50 85.00 107.50 130.00 152.50 175.00 197.50 220.00
 TIME (SECONDS) *10

Fig. VI-2. Crack Growth as a Function of Time for Specimen 7-2

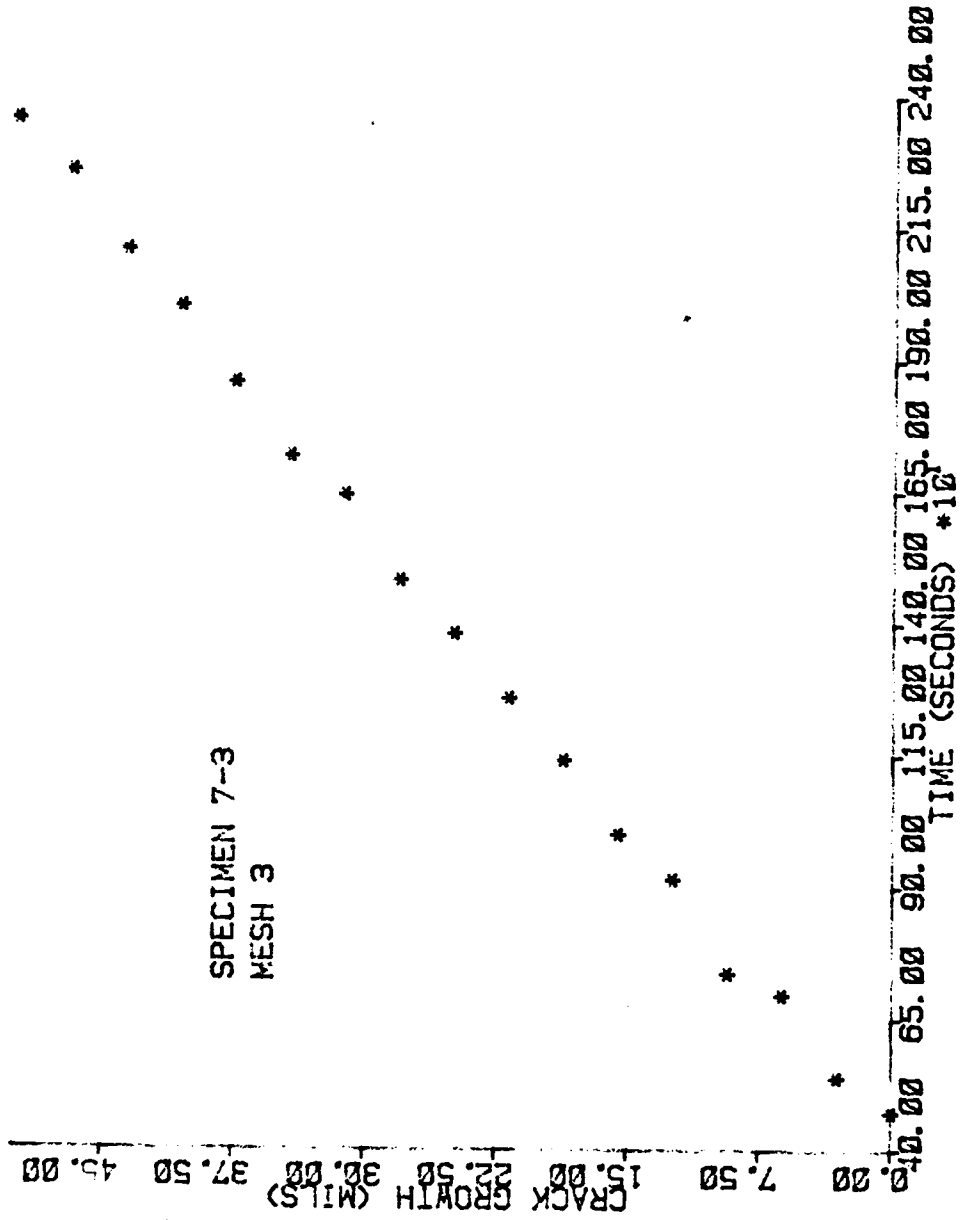


Fig. VI-3. Crack Growth as a Function of Time for Specimen 7-3

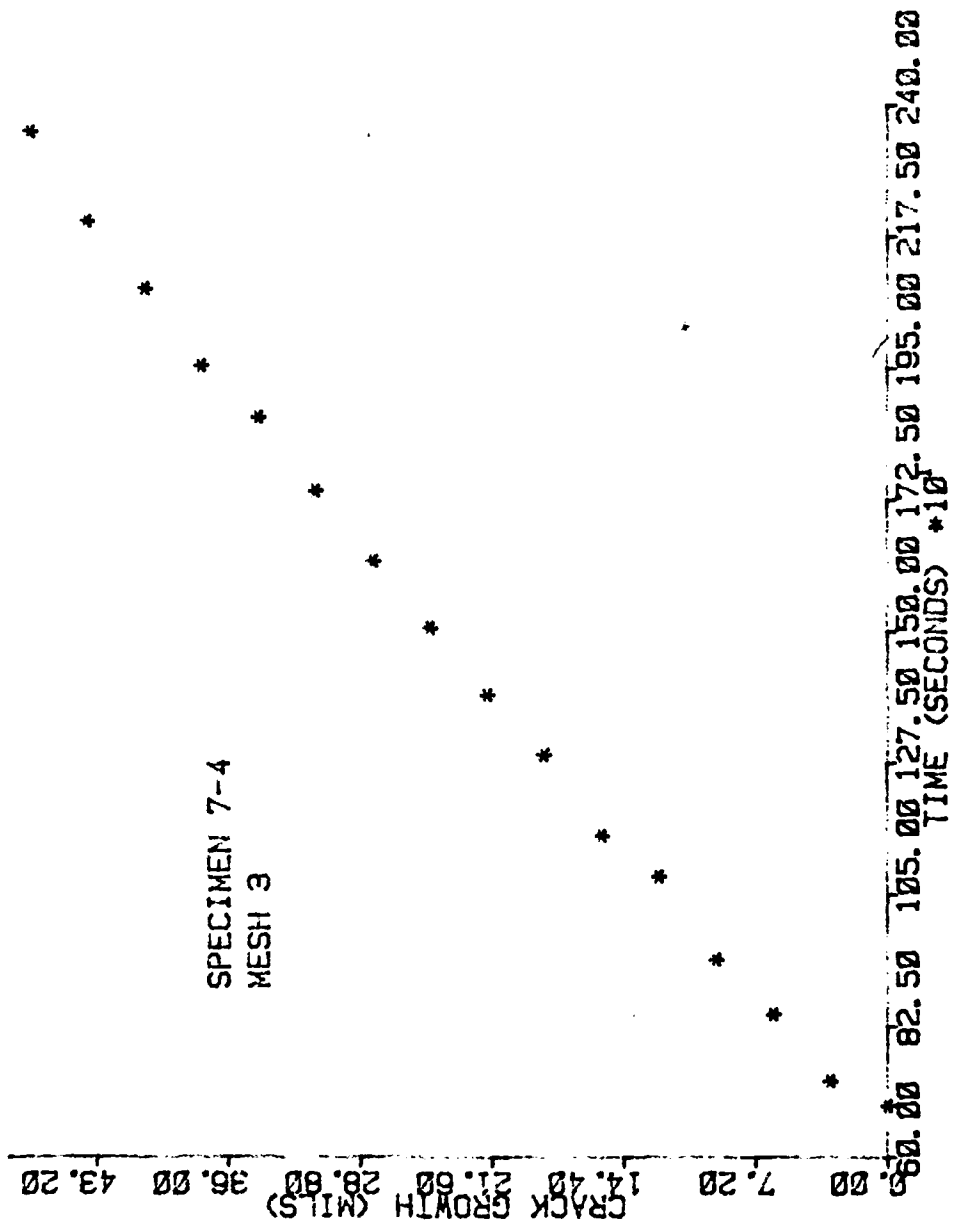


Fig. VI-4. Crack Growth as a Function of Time on Specimen 7-4

are concerned.

Notice that, after 40 minutes, both the VISCO results and the effective crack growth estimates calculated by Donath (24) are greater for specimen 7-3 than for specimen 7-4, which had a higher load. However, as shown in Table VI-1, the average crack growth rate for specimen 7-4 was greater than for specimen 7-3, so the crack growth for specimen 7-4 would have exceeded that in specimen 7-3 in a few more minutes. The difference in crack growth estimates was primarily caused by delays in the time between load application and popping of the first node to start crack growth. This time delay is taken to be the incubation period for each crack. In three out of the four cases shown in Table VI-1, an increase in load caused a corresponding increase in the crack incubation period. It is difficult to say whether this phenomenon is due to actual crack retardation or experimental scatter in the displacement data. However, temporary crack growth retardation due to the application of occasional tensile overload cycles is a well-recognized phenomenon in cyclic loading cases, and it is likely that a similar phenomenon exists for creep crack growth also.

Another thing that should be noted in Table VI-1 is that mesh 1 consistently estimated more crack growth than mesh 3. This is because finite element meshes tend to get stiffer as the size of the elements increases. Since mesh 1 is stiffer than mesh 3, it showed less displacement due to the applied load than did mesh 3. Using the HEN technique,

a stiffer mesh will show more crack growth than a fine mesh if both are forced to follow the same displacement data.

Next, compare the effective crack growth calculated by Donath with the crack growth generated by the VISCO runs. In all cases, the effective crack growth is less than that given by the VISCO runs. However, Donath showed that the effective crack length consistently underestimates the actual crack length in these tests. There is no way to tell which estimate is closer to the actual crack length. However, the amount of crack growth here was fairly small and the magnitude of the differences in crack growth estimates is, at worst, .02 in between mesh 3 and the effective crack length. Considering that the displacement measurements used to control crack growth in the models were not extremely accurate, this degree of resolution is pretty good.

Another point to consider is that, for longer runs, the difference between the effective crack length and the VISCO estimated crack length stabilized at a fairly constant value. If the two sets of crack lengths are plotted versus time, the lines run nearly parallel for the duration of the test. Thus, the crack growth rates given by the two techniques were nearly identical. This trend is illustrated in Figs. VI-5 through VI-8, where crack growth estimates generated by mesh 1 are compared to the effective crack length over the duration of each of the four tests considered. The effective crack length is not plotted on Fig. VI-6 because of inconsistencies in the published data. Note the excellent

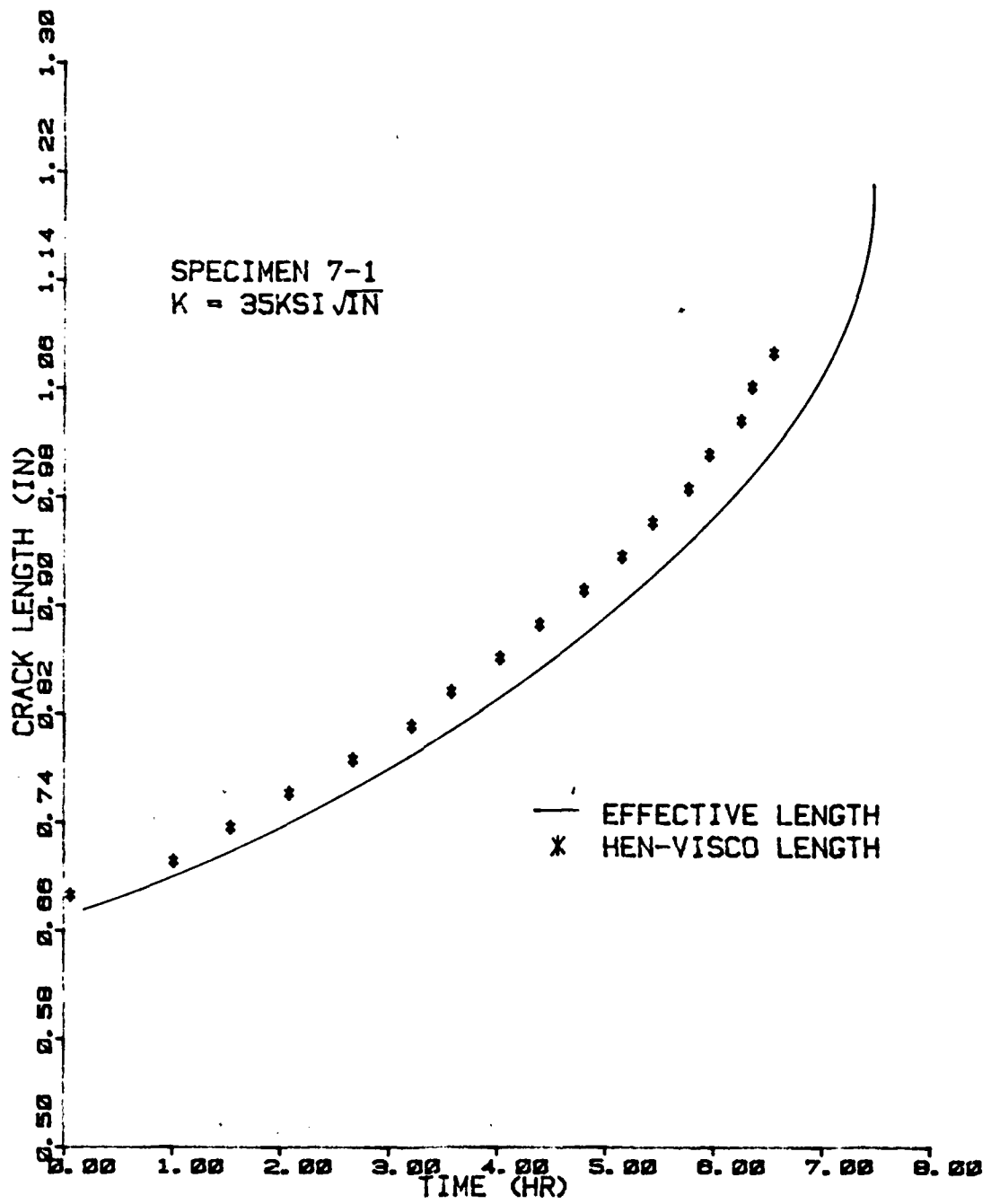
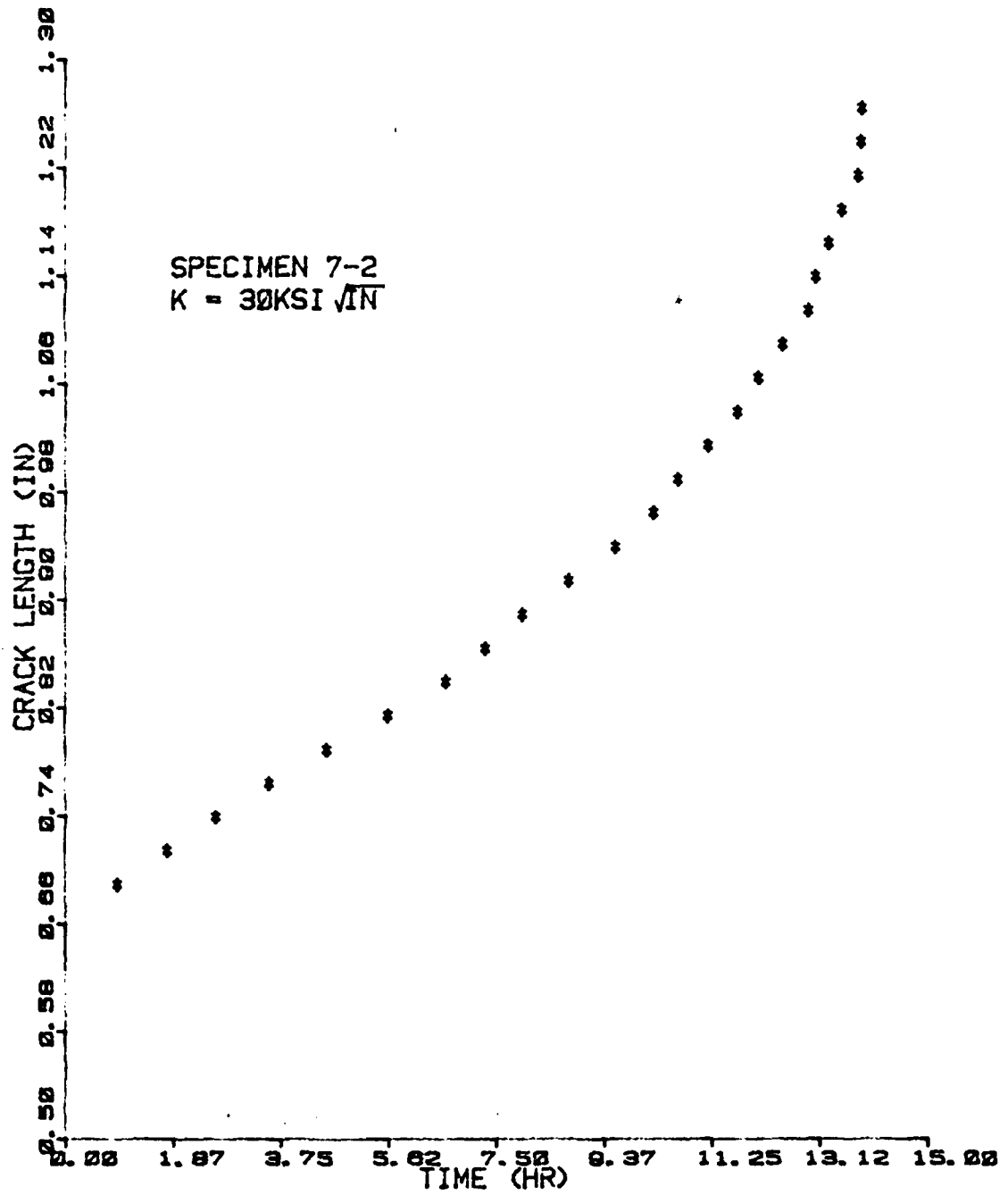


Fig. VI-5. Effective and HEN-VISCO Crack Lengths vs Time for Specimen 7-1



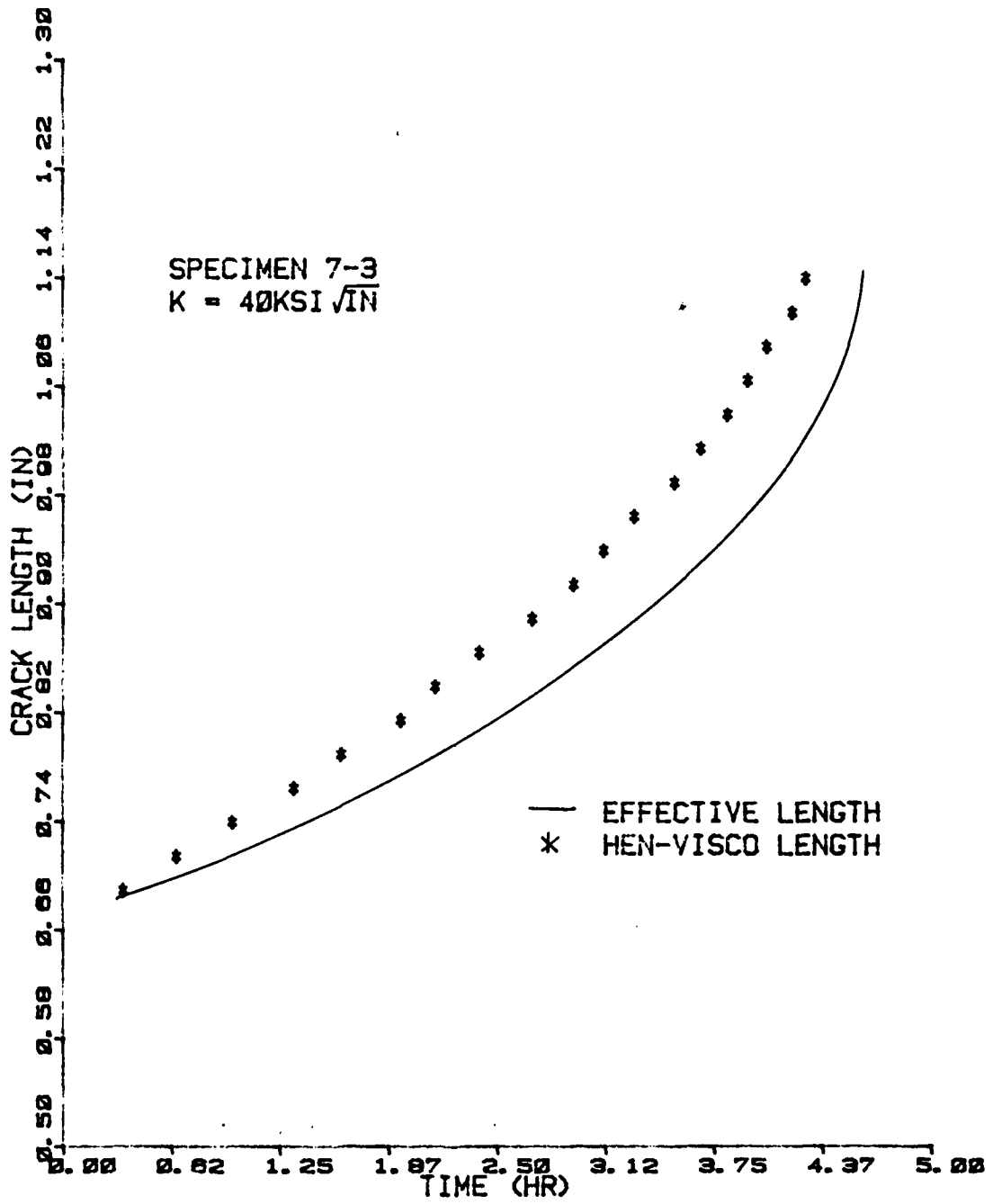


Fig. VI-7. Effective and HEN-VISCO Crack Lengths vs Time for Specimen 7-3

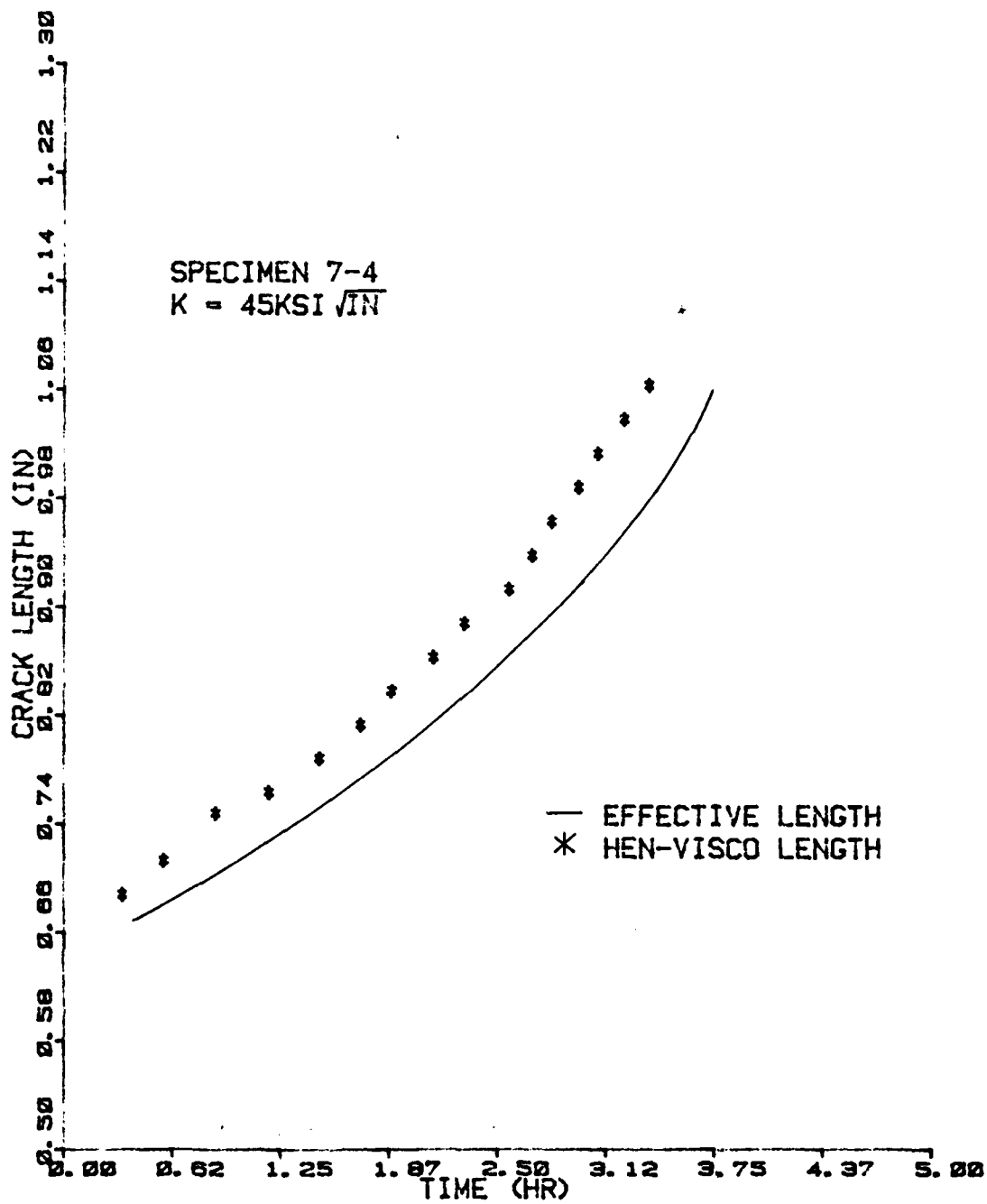


Fig. VI-8. Effective and HEN-VISCO Crack Lengths vs Time for Specimen 7-4

agreement between the VISCO results and the effective crack lengths in each case shown.

Displacement data for specimens 7-2, 3, and 4 ran out about 20 minutes before each test was actually terminated. In order to estimate what the HEN-VISCO combination would have given for a final crack length, the average crack growth rate during the last half hour of each VISCO run was used to extrapolate the estimated crack length out to test termination. Specimen 7-1 was not considered because it failed during the experimental test. Comparison of the final effective crack lengths given by Donath, the final surface crack lengths, and the final crack lengths generated by the VISCO runs are shown in Table VI-2.

TABLE VI-2

Final Crack Lengths in Test Specimens

Specimen	Test Time (min)	VISCO Simulation Time (min)	Final a Surface (in)	Final a Effective (in)	Final a VISCO (in)
7-1*	--	392	--	--	--
7-2	860	832	1.234	1.281	1.344
7-3	280	257	1.104	1.218	1.246
7-4	220	202	0.920	1.075	1.092
*failed during test					

The agreement here is excellent with the VISCO runs showing 5-10 percent more crack growth than the effective crack calculations.

Figures VI-9 through VI-11 show what the actual

fracture surface looked like when the specimens were broken open after test completion. Arrows in these figures indicate the final surface crack measurements on each side of the specimen, unlabeled lines represent the final effective crack length, and lines labeled with a "V" indicate the position of the final VISCO crack length. These figures graphically illustrate the severe tunneling that characterizes creep crack growth and the inadequacy of surface crack measurements in estimating actual crack length. Note that both the VISCO results and the effective crack lengths slightly underestimated the actual crack length, but were much more accurate than the surface crack measurements. Crack growth estimates from the VISCO runs were within 15-20 percent of the actual crack growth in every case. This amount of error is well within the limits of experimental scatter in creep crack growth tests.

Crack Growth Criteria

Based on the good correlation between predicted and actual crack growth, results from the VISCO runs were examined to see if any crack growth criteria could be formed. Parameters considered were stress, strain, effective stress and effective strain at nodes about to be released as well as the accumulated stress and strain history at each node when it was released.

Since the large stress and strain gradients near the crack tip were not displayed as well by mesh 1 as by

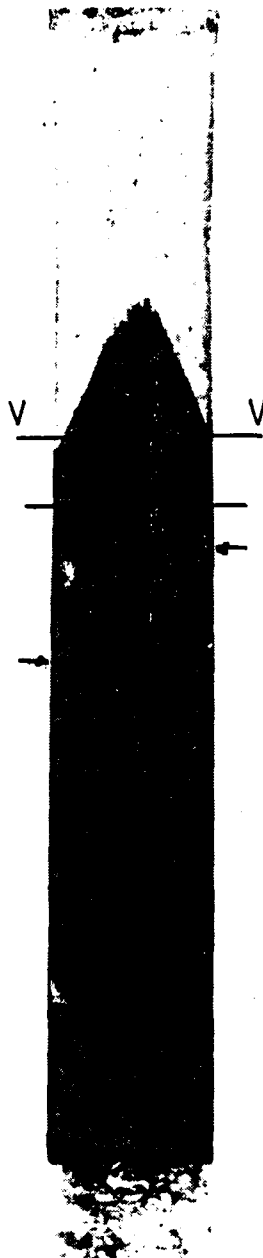


Fig. VI-9. Fracture Surface - Specimen 7-2

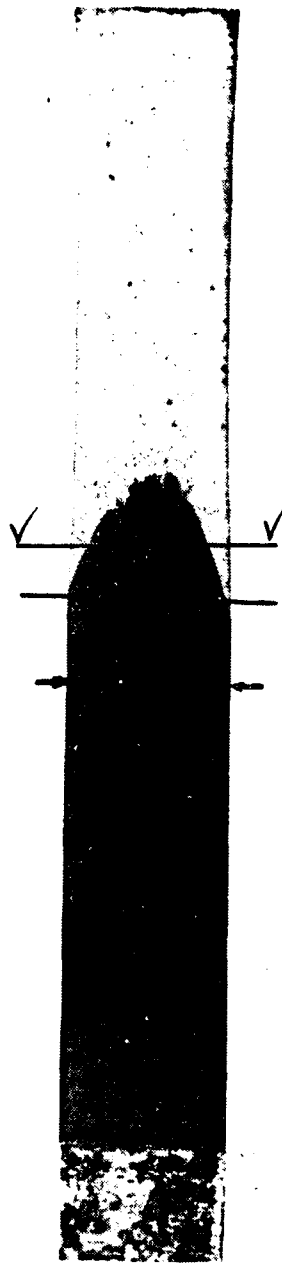


Fig. VI-10. Fracture Surface - Specimen 7-3

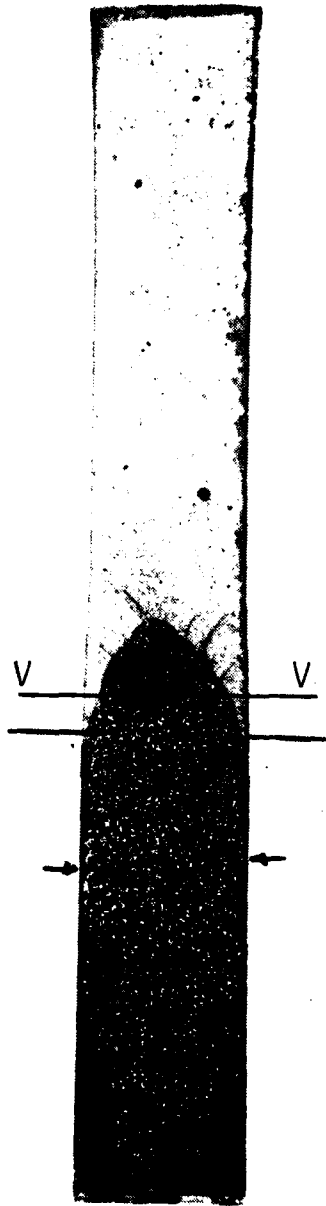


Fig. VI-11. Fracture Surface - Specimen 7-4

mesh 3, the data generated by mesh 3 were used for this phase of the investigation.

Critical Strain Criterion. Since a critical strain criterion has shown promise in previous work (32), the crack tip strains were considered first. The component of plastic strain perpendicular to the crack plane (y component) and the effective plastic strain values were each averaged for the three elements surrounding the crack tip whenever a node was about to be released. The objective was to see if some constant (critical) value of strain existed as the crack grew through each node. The calculated strain values are shown in Table VI-3. Effective strains followed the same general pattern and will not be shown. Note that in every case the strains start out high and then decrease to a steady state value as the crack grows through the specimen. Hinnerichs noted the same trend, but found that nearly all of his specimens reached a steady state value close to .03. The strains in specimens 7-3 and 7-4 both stabilized at values close to .03 but, since the element size used here was four times larger than Hinnerichs' elements, this was felt to be mostly coincidence. In any case, the strain values for specimens 7-1 and 7-2 stabilized at values much lower than .03. It appears that, with the compact tension specimens used herein, no single value of strain can be considered to control crack growth.

Critical Stress Criterion. Using the same procedure as for the strains, the average values of stress perpendicular

AD-A111 186

AIR FORCE INST OF TECH WRIGHT-PATTERSON AFB OH SCHOO—ETC F/S 12/1
THE VISCOPLASTIC CRACK GROWTH BEHAVIOR OF A COMPACT TENSION SPE—ETC(U)
DEC 81 J W SMAIL
AFIT/DAE/AA/81D-28

UNCLASSIFIED

ML

2
12
201176

END

DATE

FILMED

1982

DTIC

TABLE VI-3

Average Plastic Strain at the Crack Tip
as a Function of Crack Growth

# of Nodes Released	ϵ_y^P			
	7-1	7-2	7-3	7-4
1	.0275	.0201	.0396	.0528
2	.0274	.0174	.0363	.0462
3	.0243	.0175	.0320	.0393
4	.0231	.0169	.0260	.0318
5	.0226	.0182	.0285	.0336
6	.0215	.0205	.0269	.0311
7	.0220	---	.0273	.0318
8	.0212	---	.0268	.0310
9	.0218	---	.0266	.0310
10	.0220	---	.0263	.0312
11	.0212	---	.0271	.0311
12	.0219	---	.0255	.0312
13	.0208	---	.0265	.0302
14	---	---	.0273	.0314
15	---	---	.0262	.0311
16	---	---	.0269	.0319
17	---	---	.0261	---

to the crack plane (y component) and effective stress were calculated for nodes about to be released in each specimen. These results are shown in Tables VI-4 and VI-5. Both the effective stress and the y component of stress were nearly constant in each specimen as the crack progressed through the mesh. In addition, very little variation was noted between specimens. Note that while the load increased by 50 percent from specimen 7-2 to 7-4, both the y component of stress and the effective stress increased by less than 5 percent at nodes being released. It would seem that, at least for the specimens considered here, crack growth could be controlled by releasing nodes when the average stress at the crack tip reached a value of about 133 ksi, which is roughly equal to the yield stress. This value of stress is only about 2 percent different than the average values of either the y component of stress or the effective stress at nodes being released in each of the four specimens considered here. It should be noted, however, that the behavior patterns of the y component of stress and the effective stress are quite different.

In the case of the y component, the average stress in the three elements surrounding a node initially increases to a value well above 133 ksi as the crack approaches the node. However, when the crack actually reaches the node, the average stress will have begun to decrease due to the unloading of the previous node. It appears that the node pops when the stress relaxes to approximately 133 ksi, and

TABLE VI-4

Average Stress Perpendicular to the Crack Tip
as a Function of Crack Growth

# of Nodes Released	σ_y (ksi)			
	7-1	7-2	7-3	7-4
1	134	129	133	131
2	132	141	136	141
3	132	131	133	135
4	131	133	144	136
5	130	127	133	135
6	133	118	136	138
7	130	---	134	135
8	132	---	134	136
9	131	---	135	136
10	130	---	135	135
11	132	---	133	136
12	130	---	136	135
13	133	---	134	137
14	---	---	133	135
15	---	---	135	136
16	---	---	133	134
17	---	---	136	---
Average	131	130	135	136

TABLE VI-5

Effective Stress as a Function of Crack Growth

# of Nodes Released	$\sigma_{eff}(ksi)$			
	7-1	7-2	7-3	7-4
1	128	123	127	126
2	131	145	138	145
3	131	131	133	135
4	131	133	149	137
5	130	126	132	135
6	133	117	137	135
7	130	---	134	137
8	133	---	135	136
9	130	---	135	136
10	131	---	136	136
11	132	---	133	136
12	129	---	138	138
13	133	---	134	136
14	---	---	134	136
15	---	---	136	135
16	---	---	134	---
17	---	---	136	---
Average	131	129	135	136

the process then repeats itself for the next node.

In the case of the effective stress, the stress followed a monotonically increasing pattern and the nodes popped when the average value first reached 133 ksi or something close to this. The less complicated behavior of the effective stress would make a criterion based on it slightly easier to incorporate in a computer program than one based on the y component of stress.

Accumulated Stress/Strain History. Since it is probable that crack growth is caused not just by the level of stress or strain in a body, but by an interaction of these states and the length of time they exist at the crack tip, it was thought that equations of the following form might provide a usable crack growth criterion.

$$\int \sigma^n dt = C_1 \quad (\text{VI-1})$$

$$\int \epsilon^n dt = C_2 \quad (\text{VI-2})$$

where C_1 and C_2 are constant values that, when reached, indicate that crack growth should proceed. Eq (VI-1) is similar to the life fraction rule discussed by Goodall and Chubb (33).

Only effective stress and effective strain were investigated for use with Eqs (VI-1) and (IV-2). Also, since it seemed logical that crack growth would be dominated by the near-field stresses and strains, only the area close to the crack tip was considered. The diameter of the plastic zone surrounding the crack tip in the specimen with the highest load was chosen as the distance for which the stress and strain histories would be tracked for all specimens.

For example, the plastic zone in specimen 7-4 extended approximately 4 nodes in front of the crack tip. Thus, when the crack reached the 4th node in front of any given node, the stress or strain history was considered to start. Eq (VI-1) or (VI-2) was used to compute the area under the stress or strain versus elapsed time curve until the crack reached the node of interest. At this point, the process was stopped and the final result noted. Values of the exponent n of 1, 2 and 3 were considered.

It was found that values given by Eq (VI-1) were nearly constant for each specimen except for 7-2, but they varied widely from specimen to specimen. For the case $n = 1$, the average values given by Eq (VI-1) are shown in Table VI-6. Results for $n = 2$ and $n = 3$ followed similar patterns with the percent difference between specimens remaining nearly constant. Values for the accumulated strain history given by Eq (VI-2) varied even more widely than the stress history results shown in Table VI-6.

TABLE VI-6

Average Accumulated Stress History at Node Release for a Fixed Distance in Front of the Crack Tip

Specimen	$\int \sigma_{eff} dt \times 10^5$ psi-sec
7-1	9.23
7-2	13.86
7-3	6.35
7-4	6.00

The strain history seemed to offer little hope of providing a usable crack growth criteria, but the stress history exhibited an interesting pattern. Since the values given by Eq (VI-1) increased as the load on the specimen decreased, it seemed to indicate that too much distance in front of the crack tip was being considered for the lower load cases. Thus, instead of tracking the stress history for a fixed distance in front of the crack tip, the distance considered for each specimen was varied so that it coincided with the diameter of the plastic zone in that specimen. For specimens 7-3 and 7-4, this distance spanned approximately 4 nodes in front of the crack tip, while for specimens 7-1 and 7-2, it spanned 3 and 2 nodes respectively.

When the strain histories were recalculated using this technique, Eq (VI-1) gave the values shown in Table VI-7.

TABLE VI-7

Average Accumulated Stress History at Node Release for Plastic Zone in Each Specimen

Specimen	$\int \sigma_{eff} dt \times 10^5$ psi-sec
7-1	6.72
7-2	6.08
7-3	6.35
7-4	6.00

It appears that we are approaching a constant value that could be used as a crack growth criterion. Note that, while only the average values of the accumulated stress

history are shown in Table VI-7, the individual nodal values in three out of the four test specimens showed only minor deviations from the average. However, values for specimen 7-2 ranged from 2.43×10^5 to 16.7×10^5 psi-sec. Insufficient data exists to make a definite conclusion about the accuracy of this technique, but it looks promising and merits further investigation.

VII. Summary and Conclusions

A two-dimensional plane stress/plane strain finite element program called VISCO was used to model creep crack growth in IN-100 at 1350 F. The constitutive equations employed in VISCO were in the form of a sophisticated, non-linear, time dependent material model developed by Bodner and Partom. This model accurately predicts material behavior during both primary and secondary creep.

The hybrid experimental numerical procedure was used to predict creep crack growth in four different compact tension specimens under loads that produced stress intensity factors ranging from 30 to 45 ksi in^{1/2}.

Several crack growth criteria were investigated in an effort to determine the parameters that control creep crack growth.

The following statements and conclusions are based on the analysis presented in this paper:

1. The HEN procedure, when coupled with the VISCO computer program, provides good estimates of creep crack growth in compact tension specimens when easily measured, far field displacements are used as the experimental input. Results compared favorably to those obtained by Hinnerichs using near field displacements in center cracked plates. It appears that, unless the user wishes to resolve very small increments

of crack growth, extremely accurate displacement measurements are not required. The degree of accuracy provided by measurements taken with LVDT's was sufficient for the analysis conducted herein.

2. Constant strain triangular elements work well for resolving both small and large increments of creep crack growth. In addition, extremely fine meshes are not required to obtain good estimates of crack growth over the range of behavior considered in this study. A mesh with crack tip elements roughly 32 times the size of IN-100 grains was able to predict crack growth to within 15-20 percent of actual growth over periods ranging from 5 to 14 hours.

3. Both crack length estimates from the VISCO computer program and effective crack lengths calculated from compliance measurements give much more accurate indications of true crack length than do surface crack measurements.

4. The stress transmitted to the crack tip in a finite element model of a compact tension specimen is not highly dependent on the mesh refinement in the area above the load application point. Refinement of the mesh in the area around the crack tip does effect results, but convergence is very slow once the elements reach approximately .025 inches in size.

5. No single value of strain for a critical strain crack growth criterion was found to match the conditions in all of the specimens considered herein. An accumulated strain history parameter also proved ineffective. However, the

stress level of nodes being released was nearly constant in every specimen which indicated that a critical stress criterion holds promise as a crack growth parameter. Encouraging results were also obtained with an accumulated stress history criterion where the area under the stress versus elapsed time curves was tracked for each node in the plastic zone surrounding the crack tip as the crack grew through the specimen. Use of this criterion merits further investigation to see if it can be applied to different specimen geometries and to wide ranges of load levels.

It is believed that the crack growth estimates and criteria presented herein will add to the body of knowledge concerning high temperature crack propagation and provide progress towards life prediction of actual turbine disks.

Bibliography

1. Collins, J.A. Failure of Materials in Mechanical Design. New York: John Wiley & Sons, 1981.
2. Harris, J.A., Jr., D.L. Sims, C.G. Annis, Jr. "Concept Definition: Retirement for Cause of F-100 Rotor Components." AFWAL-TR-80-4118, Wright-Patterson AFB, Ohio, 1980.
3. Bodner, S.R., and Y. Partom. "Constitutive Equations for Elastic-Viscoplastic Strain Hardening Materials," Journal of Applied Mechanics Trans., 42:385-389 (1975).
4. Bodner, S.R. "Representation of Time Dependent Mechanical Behavior of Rene 95 By Constitutive Equations," AFML-TR-79-4116, Wright-Patterson AFB, Ohio, 1979.
5. Stouffer, D.C., and S.R. Bodner. "A Relationship Between Theory and Experiment for a State Variable Constitutive Equation," AFWAL-TR-80-4194, Wright-Patterson AFB, Ohio, 1981.
6. Stouffer, D.C. "A Constitutive Representation for IN-100," AFWAL-TR-81-4039, Wright-Patterson AFB, Ohio, 1981.
7. Zienkiewicz, O.C., and I.C. Corneau. "Visco-Plasticity -- Plasticity and Creep in Elastic Solids: A Unified Numerical Solution Approach," International Journal for Numerical Methods in Engineering, 8:821-845 (1974).
8. Armen, H. "Assumptions, Models, and Computational Methods for Plasticity," Computers and Structures, 10: 161-174 (1979).
9. Hinnerichs, T.D. "Viscoplastic and Creep Crack Growth Analysis by the Finite Element Method." PhD Dissertation, Department of Aeronautics and Astronautics, Air Force Institute of Technology, Wright-Patterson AFB, Ohio, 1980.
10. Bathe, K.J., and E.L. Wilson. Numerical Methods in Finite Element Analysis. Chapter 7, pp. 291-294. Englewood Cliffs, N.J.: Prentice-Hall, Inc., 1976.
11. Zienkiewicz, O.C. The Finite Element Method (Third Edition). Chapter 24, pp. 724-726. New York: McGraw-Hill Book Company, 1977.

12. Jennings, Alan. Matrix Computation for Engineers. Chapter 6, pp. 182-188. New York: John Wiley & Sons, 1977.
13. Spencer, C.G. Introduction to Plasticity. London: Chapman & Hall, Ltd., 1968.
14. Lubahn, J.D., and R.P. Felgar. Plasticity and Creep of Metals. New York: John Wiley & Sons, 1961.
15. Dieter, George E., Jr. Mechanical Metallurgy. New York: McGraw-Hill Book Company, 1961.
16. Mendelson, Alexander. Plasticity: Theory and Application. New York: The Macmillan Co., 1968.
17. Bridgman, P.W. "The Effect of Hydrostatic Pressure on the Fracture of Brittle Substances," Journal of Applied Physics, 18:246 (1947).
18. Bridgman, P.W. Studies in Large Plastic Flow and Fracture with Special Emphasis on the Effects of Hydrostatic Pressure. New York: McGraw-Hill Book Company, 1952.
19. Clauss, Francis J. Engineers' Guide to High Temperature Materials. Reading, Mass.: Addison-Wesley Publishing Company, 1969.
20. Westergaard, H.M. Theory of Elasticity and Plasticity. Boston: Harvard University Press, 1952.
21. Andrade, E.N. da C. Viscosity and Plasticity. New York: Chemical Publishing Co., Inc., 1951.
22. Andrade, E.N. da C. Creep and Recovery. Metals Park, Oh.: American Society for Metals, 1957.
23. Zienkiewicz, O.C., and I.C. Corneau. "Visco-Plasticity by Finite Element Process," Archives of Mechanics, 24: 873-889 (1972).
24. Donath, R.C. "Crack Growth Behavior of Alloy IN-100 Under Sustained Load at 732 C (1350 F)." AFWAL-TR-80-4131, Wright-Patterson AFB, Ohio, 1981.
25. Rolfe, S.T., and J.M. Barsom. Fracture and Fatigue Control in Structures. Chapter 2, pp. 30-47. Englewood Cliffs, N.J.: Prentice-Hall Inc., 1977.
26. Mills, W.J., L.A. James, and J.A. Williams. "A Technique for Measuring Load Line Displacements of Compact Ductile Fracture Toughness Specimens at Elevated Temperatures," Journal of Testing and Evaluation, 5(6): 446-451 (November 1977).

27. Ohtani, R., and S. Nakamura. "Crack Propagation in Creep (Finite Element Analysis)," Journal of the Society of Materials Science, 25(275): August 1976.
28. Tada, H. The Stress Analysis of Cracks Handbook. Hellertown, Pa.: Del Research Corporation, 1973.
29. Atluri, S.N., and M. Nakagaki. "J-Integral Estimates for Strain-Hardening Materials in Ductile Fracture Problems," AIAA Journal, 15(7):923-931 (1977).
30. Chan, S.K., I.S. Tuba, and W.K. Wilson. "On the Finite Element Method in Linear Fracture Mechanics," Engineering Fracture Mechanics, 2:1-17 (1970).
31. Kobayashi, A.S. "Current and Future Experimental Methods," Fracture Mechanics, edited by N. Perrone, H. Liebowitz, D. Mulville, and W. Pilkey. Tenth Symposium on Naval Structural Mechanics, Washington, 1978.
32. Belie, R.G., and J.N. Reddy. "Direct Prediction of Fracture for Two Dimensional Plane Stress Structures," Computers and Structures, 11:49-53 (1980).
33. Goodall, I.W., and E.J. Chubb. "The Creep Ductile Response of Cracked Structures," International Journal of Fracture, 12(2):(April 1976).

APPENDIX

Finite Element Formulation

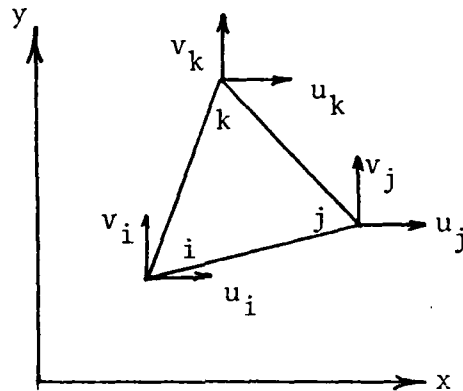


Fig. A-1. Constant Strain Triangular Element

As illustrated in Fig. A-1, the behavior of a constant strain triangular element is described by six degrees of freedom.

$$\{U\} = [u_i \ v_i \ u_j \ v_j \ u_k \ v_k]^T \quad (A-1)$$

where the u and v parameters represent displacements in the x and y directions of each individual node. These displacement parameters can be expressed in the form of a linear polynomial such that

$$\begin{aligned} u &= \alpha_1 + \alpha_2 x + \alpha_3 y \\ v &= \alpha_4 + \alpha_5 x + \alpha_6 y \end{aligned} \tag{A-2}$$

where the α_i are constants determined from the nodal displacements and nodal coordinates as

$$\begin{Bmatrix} \alpha_1 \\ \alpha_2 \\ \alpha_3 \end{Bmatrix} = \frac{1}{2A} \begin{bmatrix} a_i & a_j & a_k \\ b_i & b_j & b_k \\ c_i & c_j & c_k \end{bmatrix} \begin{Bmatrix} u_i \\ u_j \\ u_k \end{Bmatrix} \tag{A-3}$$

and

$$\begin{Bmatrix} \alpha_4 \\ \alpha_5 \\ \alpha_6 \end{Bmatrix} = \frac{1}{2A} \begin{bmatrix} a_i & a_j & a_k \\ b_i & b_j & b_k \\ c_i & c_j & c_k \end{bmatrix} \begin{Bmatrix} u_i \\ u_j \\ u_k \end{Bmatrix} \tag{A-4}$$

where A is the area of the element. The coefficients a_i , b_i , and c_i are given by

$$\begin{aligned} a_i &= x_i y_k - x_k y_j \\ b_i &= y_j - y_k \\ c_i &= x_k - x_j \end{aligned} \tag{A-5}$$

with the other coefficients determined by cyclic permutation of the subscripts i , j , and k .

The strains at any point within an element can be defined in terms of the derivatives of the displacements as

$$\{\epsilon\} = \begin{Bmatrix} \epsilon_x \\ \epsilon_y \\ \gamma_{xy} \end{Bmatrix} = \begin{Bmatrix} \frac{\partial u}{\partial x} \\ \frac{\partial v}{\partial y} \\ \frac{\partial u}{\partial y} + \frac{\partial v}{\partial x} \end{Bmatrix} \tag{A-6}$$

If we substitute Eqs (A-2) to (A-5) into Eq (A-6), the strains can be written in terms of the nodal displacements and nodal coordinates as

$$\{\epsilon\} = [B]\{U\} \quad (A-7)$$

where $\{U\}$ is defined in Eq (A-1) and

$$[B] = \frac{1}{2A} \begin{bmatrix} b_i & 0 & b_j & 0 & b_k & 0 \\ 0 & c_i & 0 & c_j & 0 & c_k \\ c_i & b_i & c_j & b_j & c_k & b_k \end{bmatrix} \quad (A-8)$$

The matrix $[B]$ is called the strain-displacement matrix.

Once the strains are known, we can calculate the stresses as follows:

$$\{\sigma\} = [D]\{\epsilon\} \quad (A-9)$$

where $[D]$ is called the elastic material property matrix.

For the case of plane stress, this matrix becomes

$$[D] = \frac{E}{1-\nu^2} \begin{bmatrix} 1 & \nu & 0 \\ \nu & 1 & 0 \\ 0 & 0 & \frac{1-\nu}{2} \end{bmatrix} \quad (A-10)$$

Finally, the elastic response of the element can be given by

$$[K]\{U\} = \{P\} \quad (A-11)$$

where $[K]$ is the elastic stiffness matrix, $\{U\}$ is the displacement vector, and $\{P\}$ represents the applied loads. The exact form of $[K]$ is

$$[K] = \sum_{m=1}^M \int [B]^T [D] [B] d \text{ vol} \quad (A-12)$$

where the summation is carried out over all the elements in the structure and the integration takes place over the area of each individual element.

If the stresses are known, the nodal forces can be calculated from the relation

$$\{f\} = \sum_{m=1}^M \int [B]^T \{\sigma\} d \text{ vol} \quad (\text{A-13})$$

Nodal forces due to known strain states are given by

$$\{f\} = \sum_{m=1}^M \int [B]^T [D] \{\epsilon\} d \text{ vol} \quad (\text{A-14})$$

Vita

James W. Smail was born on 25 February 1950 in Springfield, Massachusetts. He graduated from Cathedral High School in 1968 and attended the United States Air Force Academy, where he received his B.S. in Engineering Mechanics in June 1972. Upon graduation from the Academy, he was commissioned as a second lieutenant in the USAF. He attended undergraduate pilot training at Moody AFB, Georgia and earned his wings in October 1973. He then served as a B-52 pilot with the 596th Bombardment Squadron at Barksdale AFB, Louisiana until May 1980. While serving as an aircrew member, he took course work from the University of Southern California that led to his M.S. in Systems Management in 1978. He entered the School of Engineering, Air Force Institute of Technology in June 1980.

UNCLASSIFIED

SECURITY CLASSIFICATION OF THIS PAGE (When Data Entered)

REPORT DOCUMENTATION PAGE		READ INSTRUCTIONS BEFORE COMPLETING FORM
1. REPORT NUMBER AFIT/GAE/AA/81D-28	2. GOVT ACCESSION NO.	3. RECIPIENT'S CATALOG NUMBER
4. TITLE (and Subtitle) THE VISCOPLASTIC CRACK GROWTH BEHAVIOR OF A COMPACT TENSION SPECIMEN USING THE BODNER-PARTOM FLOW LAW		5. TYPE OF REPORT & PERIOD COVERED Master's Thesis
		6. PERFORMING ORG. REPORT NUMBER
7. AUTHOR(s) James W. Smail Capt. USAF		8. CONTRACT OR GRANT NUMBER(s)
9. PERFORMING ORGANIZATION NAME AND ADDRESS Air Force Institute of Technology (AFIT/EN) Wright-Patterson AFB, Ohio 45433		10. PROGRAM ELEMENT, PROJECT, TASK AREA & WORK UNIT NUMBERS
11. CONTROLLING OFFICE NAME AND ADDRESS Air Force Institute of Technology (AFIT/EN) Wright-Patterson AFB, Ohio 45433		12. REPORT DATE December 1981
		13. NUMBER OF PAGES 113
14. MONITORING AGENCY NAME & ADDRESS (if different from Controlling Office)		15. SECURITY CLASS. (of this report) UNCLASSIFIED
		15a. DECLASSIFICATION/DOWNGRADING SCHEDULE
16. DISTRIBUTION STATEMENT (of this Report) Approved for public release; distribution unlimited.		
17. DISTRIBUTION STATEMENT (of the abstract entered in Block 20, if different from Report) Air Force Institute of Technology (AFIT/EN) Wright-Patterson AFB, OH 45433		
18. SUPPLEMENTARY NOTES Approved for public release; IAW AFR 190-17 <i>Frederic C. Lynch</i> Frederic C. Lynch, Major, USAF 28 JAN 1982 Director of Public Affairs		
19. KEY WORDS (Continue on reverse side if necessary and identify by block number) Finite Elements Bodner-Partom Flow Law Viscoplastic High Temperature Crack Growth		
20. ABSTRACT (Continue on reverse side if necessary and identify by block number) Creep crack growth in IN-100 was studied using a hybrid experimental-numerical procedure (HEN). This procedure couples displacement data generated during creep crack growth tests to a finite element model of the test specimen. A standard compact tension specimen geometry was used in all cases. The computer program used herein is a two-dimensional plane stress/plane strain code that uses constant strain		

DD FORM 1473

EDITION OF 1 NOV 65 IS OBSOLETE

UNCLASSIFIED

SECURITY CLASSIFICATION OF THIS PAGE (When Data Entered)

UNCLASSIFIED

SECURITY CLASSIFICATION OF THIS PAGE (When Data Entered)

Block 20:

triangular elements and has the ability to release fixed nodes to simulate crack growth. This procedure is facilitated by using a Gauss-Seidel iterative solution technique that allows appropriate terms in the stiffness matrix to be changed between timesteps to accommodate changing boundary conditions due to crack growth. A variable timestep algorithm maximizes the timestep size during the analysis while maintaining good accuracy.

Constitutive equations proposed by Bodner and Partom were used to account for the nonlinear, viscoplastic material behavior exhibited by IN-100 at high temperatures. These equations were integrated through time by a linear Euler extrapolation technique.

Crack growth estimates generated with the HEN procedure were within 20 percent of the actual crack growth in the test specimens after times ranging from 5-14 hours. Additionally, a critical stress and an accumulated stress history criterion for crack growth were both found to show promise. Both of these criteria merit further investigation.

UNCLASSIFIED

SECURITY CLASSIFICATION OF THIS PAGE (When Data Entered)

FILMED
— 8